Universität Hamburg
DER FORSCHUNG | DER LEHRE | DER BILDUNG

Master Thesis in Physics

Dynamical Control of Quantum Josephson Junction

By

Nicolas Tobias Heimann

June 2019

Supervisor: Prof. Dr. Ludwig Mathey
Zentrum für optische Quantentechnologien und Institut für Laserphysik, Universitat Hamburg
Second Referee: Prof. Dr. Andrea Cavalleri
Max-Planck-Institut fur Struktur und Dynamik der Materie, Hamburg
Department of Physics, Clarendon Laboratory, University of Oxford

Abstract

In this work we analyze a quantum model of a single Joseph junction in the electromagnetic field. Dissipation is implemented by emission and absorption of photons thru dipole coupling. We developed a software package, which is capable of integrating the equations of motion of the system. Numerical pump-probe experiments are implemented in an additional framework, which forms the base of the numerical analysis within this thesis. At low frequencies, the response of the system is in harmony with the London theory of superconductivity. It turns out that at even lower frequencies, the response corresponds to a Drude electron gas which we associate with uncertainty of modes. Finite temperatures allow to activate thermal modes which manifest thru additional zero-crossings in the response. The Josephson energy is modulated parametrically by an additional optical potential. Numerical analysis shows that the superconducting response is enhanced if the modulation frequency is blue-detuned to the longitudinal plasma frequency. Thermal modes may couple to the modulation due to which a significant enhancement of the superconductive response can be observed.

Zusammenfassung

In dieser Arbeit wird ein quantenmechanisches Model der Josephson Junction im elektromagnetischen Feld untersucht. Dämpfungsprozesse werden durch Emission und Absorption von Photonen mittels Dipolwechselwirkung realisiert. Ein eigens entwickeltes Softwarepaket ist in der Lage die Bewegungsgleichungen in der Zeit zu integrieren. Numerische pump-probe Experimente werden in einem zusätzlichen Framework implementiert und liegen den numerischen Analysen dieser Arbeit zu Grunde. Im niederfrequenten Spektrum stimmt die Antwort des Systems zunächst mit der London Theorie eines Supraleiters überein. Bei tieferen Frequenzen allerdings entspricht die Antwort der Drude-Theorie, welche wir mit einer Unbestimmtheit der Ladungszustände assoziieren. Endliche Temperaturen erlauben es thermische Moden zu öffnen, welche sich in der Antwort als Nulldurchgänge manifestieren. Die Josephson Energie wird durch ein zusätzliches optisches Potential parametrisch modelliert. In numerischen Betrachtungen beobachten wir eine verstärkte supraleitende Antwort, falls die Modulationsfrequenz blauverstimmt zur longitudinalen Plasmafrequenz ist. Thermische Moden koppeln an diese Modulation, wodurch eine signifikante Verstärkung der supraleitenden Antwort beobachtet werden kann.

Contents

Chapter 1

Introduction

High temperature superconductivity has become a rich and recent topic in condensed matter physics. In 1986, Bednorz and Müller discovered that barium-lanthanum-cupper-oxide becomes a superconductor at temperatures $\sim 30K$ [BM86]. Shortly afterwards, Torng et al. discovered that yttrium-barium-copper-oxide (YBCO) goes into superconductive phase at $\sim 90K$ [WAT$^+$87]. A common feature such *cuprate superconductors* share are layers of copper-oxide (CuO) planes. From a theoretical perspective, the CuO layers host condensed Cooper pairs and are weakly coupled along the c-axis [Leg06]. The Lawrence-Doniac model provides phenomenological insights as it describes the layers by weakly coupled Josephson junctions [CB12].

Recent pump-probe experiments attracted attention as they allow to study the dynamical properties of high temperature superconductors. Cavaleri et al. showed that driving of an optical photon mode transiently enhances the inter-bilayer coherent c-axis transport of an YBCO [FTD$^+$11, HKN$^+$14]. Several studies on effective bilayer systems of parametrically driven Josephson junctions showed an enhanced effective bilayer coupling from a theoretical perspective [HZR$^+$15, OCM16a, OHCM17, Hom18].

In this thesis, a quantum mechanical treatment of a single Josephson junction is presented. The quantum Josephson junction implements dissipation processes by emission and absorption of photons from a heat bath. As we assume the weak coupling limit, a quantum dynamical semigroup describes the dynamics. The core of the numerical analysis is a GPU based solver of general weak coupling master equations. A framework to numerically perform pump-probe experiments is implemented. Non-equilibrium states from zero to high temperature configurations are then analyzed.

This thesis is structured as follows: Chapter 2 gives a brief history on the discovery of superconductivity. Then, an overview of the basic theories describing superconductivity is provided. In Chapter 3 a brief introduction to open quantum system is given. A quantum dynamical semigroup is constructed by asserting weak coupling conditions. A technical

documentation of the numerical implementation, as well as basic assumptions to enhance computational performance, are presented. In Chapter 4, the quantum model of the Josephson junction, which couples as a dipole to the electromagnetic field, is set up. Equilibrium configurations are then analyzed by a numerical treatment. In Chapter 5, the low frequency response in numerical pump-probe experiments is dynamically controlled. Chapter 6 finally summarizes the results of this work.

Chapter 2

Basic theory

An electrical conductor is a material in which charges are able to flow as an electrical current. It is not that the distinct charges move across the whole conductor, rather they transfer momentum to other delocalized charges, forming a charged gas drifting through the material. The ability to let an electrical current I flow through the conductor, under the presence of an electrical potential difference V, is the *conductivity* $\sigma = I/V$. The reciprocal to the conductivity is the resistance R, in which terms the latter definition is known as Ohm's law $I = VR^{-1}$. Gustav Kirchhoff reformulated Ohm's law in terms of the local current density $\vec{J} = nq\vec{v}$ and the electromagnetic field $\vec{E}$

$$\vec{J}(\omega) = \sigma(\omega)\vec{E}(\omega), \tag{2.1}$$

where n is the number density of charges q and $\vec{v}$ is the drift velocity of the gas.

In the 19th century the condensation of gases into liquid phase gathered a lot of attention. Between 1823-1844, Faraday was able to liquify gases with high critical temperatures by exposing them to high pressures [LEE]. In 1873, Van der Waals proposed an equation of state of a non-ideal gas, allowing to predict the critical point of a gas, at which the density of the liquid and the gas phase match up [Kle74]. This theory allows a precise preparation of gases below the critical temperature. By increasing the pressure, a phase transition into liquid phase is triggered. A further decrease of temperature is achieved by evaporation. Next, the sample can be used to chill a gas with a lower critical temperature. Towards the end of the 19th century, Dewar used liquid nitrogen to cool unalloyed metals and discovered a saturating resistivity at low temperatures [Wis03]. The electrical properties at low temperatures attracted a lot of attention during the following years. In 1908, H. Kamerlingh Onnes was the first to liquefy helium at a temperature of $\sim 4K$. By reducing the pressure in the experimental chamber, a temperature $\sim 1K$ was achieved, which was the coldest spot on earth till then. Three years later, in 1911, Onnes observed that the resistivity of mercury disappears below a critical temperature of $T_C = 4.183K$, which was
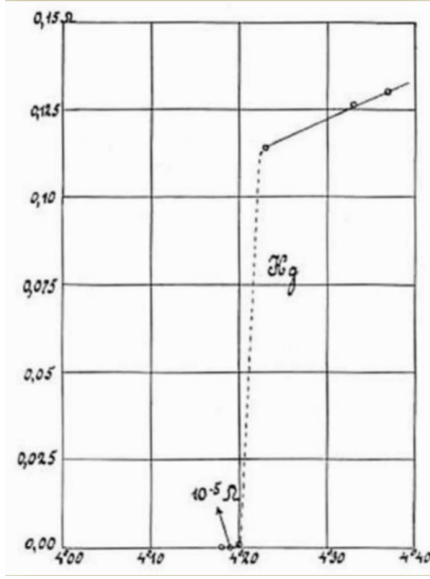
Figure 2.1: **Resistivity of mercury**
The first experimental evidence of superconductivity.
At $T \sim 4.2K$, the resistivity suddenly drops to $10^{-5}\Omega$.
Historic plot by H. Kamerlingh Onnes taken from
[DDK11].

the first evidence of superconductivity [Onn91]. Figure 2 provides the historic plot showing the disappearance of the resistivity of mercury at low temperatures. Onnes work on low temperature phenomena was honored with the Nobel prize of physics in 1913 [Onn13]. By inducing a current into a ring of lead at a temperature of 1.8K, Onnes was able to show that the material actually was a perfect conductor, since the electrical current persisted in the loop [DDK11]. Other materials, i.e. tin and lead, have lined up on the list of superconducting metals shortly thereafter.

The phenomenon of perfect conductivity attracted further interest in the upcoming years. Already in 1889, Gabriel Lippmann could classically show, that the magnetic flux is stationary in a perfect conductor [Gab89]. Therefore, the magnetic flux would be trapped as the material becomes a perfect conductor. However, in 1933 Meißner and Ochsenfeld discovered that perfect conductors also appear to be perfect diamagnets [MO33]. Spontaneous magnetization expels magnetic flux from the interior and shields the superconductor from outer fields. Superconductivity is therefore more than just an electrical property, but a phase of matter.

The first phenomenological description of superconductivity was established by the London brothers in 1935 [LLL35]. They proposed two macroscopic equations, which are known as the *London equations*

$$\vec{E} = \Lambda \frac{\partial \vec{J}}{\partial t} \qquad \vec{B} = -c\Lambda \vec{\nabla} \times \vec{J} \qquad \Lambda = \frac{m}{n_s q^2}. \qquad (2.2)$$

In these equations, m is the mass of the charge q and n_s the density of superconducting charges. The success of the London equations arises from the fact that they describe both perfect conductivity as well as the Meißner effect on a macroscopic level. Perfect conductiv-

ity is described by the first London equation; an electrical field E accelerates charge carriers in the superconductor uniformly, which corresponds to zero resistance. The Meißner effect can be quantified by using the Maxwell equations

$$\nabla \times \vec{B} = \frac{4\pi}{c}\vec{J} \qquad \vec{\nabla}\vec{B} = 0, \tag{2.3}$$

together with the second London equation. It follows that an external magnetic field is suppressed exponentially $\nabla^2\vec{B} = \lambda_L^{-2}\vec{B}$, characterized by the *London Penetration Depth*

$$\lambda_L = \sqrt{\frac{mc^2}{4\pi n_s q^2}}. \tag{2.4}$$

Even though the London theory is very successful capturing the basic phenomena of superconductivity, it cannot be derived from a microscopic perspective. In 1948, London proposed that the London equations may be a consequence of a condensed state in momentum space having long range order [Lon48]. This turned out to be on track to the first microscopic theory of superconductivity, the BCS theory.

2.1   BCS theory

Several experiments have shown that impurities in the material affect the penetration depth, while the critical temperature T_C is barely influenced. In 1953, Pippard proposed an extension to the London theory by introducing an additional length scale, the *Coherence length* ξ, describing the change of the condensate to an empty region [PB53]. His theory is in harmony with the experiment and captures the varying penetration depth. In 1955, Barden assumed that one requires a minimal energy (the gap) $\Delta \sim k_b T_c$ to excite condensed electrons near the surface of the Fermi sea. Excited electrons then contribute to the gas of normal electrons. He showed that the coherence length is a consequence of the existence of the gap [Bar55]. Soon afterwards, Cooper proposed that electrons, close the Fermi surface, may form bound states when a weak attractive force is present [Coo56]. This is the theoretical discovery of the *Cooper pair*, which turned out to be a key aspect in the microscopic picture of superconductivity.

Subsequently, Bardeen, Cooper and Schriepper formulated the BCS Theory as the first microscopic theory of superconductivity [BCS57a, BCS57b]. The BCS theory states that electrons, near the Fermi surface, of equal momentum and opposite spin, can form a bound state, due to weak attractive forces. Cooper pairs behave like bosons, thus they are able to condense into the same state as they do not obey Pauli's exclusion principle. Electrons obey the exclusion principle. Thus, breaking a Cooper pair by arbitrary small excitations, would require to reorganize the whole Fermi sea; even tiny attractive forces are sufficient for pairing electrons, since excitations below the gap Δ are ineffective. When the thermal energy drops below the gap, condensation takes place, forming a state of long range order. The condensate is transparent to excitation below the gap Δ, thus it is a superfluid corresponding to zero resistance. One mechanism which provides a net attractive force is electron$-$phonon interaction due to lattice vibrations. The size of a Cooper pair is associated with the coherence length ξ, which typically has a value of 10^3Å .

Even though the mathematical aspects of the BCS theory are rich and purposeful, they are beyond the horizon of this work. Thus, we won't go into further details at this point.

2.2   Ginzburg Laundau theory

Ginzburg and Landau achieved a striking milestone in the phenomenological description of superconducting materials [Gin55]. By introducing a complex order parameter field $\psi(\vec{r})$, spatial variations of the condensate density are resolved. Remarkably, the Ginzburg Landau (GL) theory can be derived from the BCS theory [GMB64]. The complex order parameter is given by the density of condensed electrons $n_s(\vec{r})$ and the complex phase $\phi(\vec{r})$

$$\psi(\vec{r}) = \sqrt{n_s(\vec{r})} \exp(i\phi(\vec{r})). \tag{2.5}$$

Ginzburg and Landau proposed that the free energy of the system is given in terms of powers of the order parameter $|\psi|$, a kinetic term, and the magnetic field $\vec{B} = \vec{\nabla} \times \vec{A}$

$$F = \alpha|\psi|^2 + \frac{\beta}{2}|\psi|^4 + \frac{1}{2m}\left|\left(\frac{\hbar}{i}\nabla - e_*\vec{A}\right)\psi\right|^2 + \frac{|\vec{B}|^2}{2\mu_0}. \tag{2.6}$$

By minimizing the free energy in terms of the order parameter and the vector potential, the two *Ginzburg Landau equations* arise

$$\alpha\psi + \beta|\psi|^2\psi + \frac{1}{2m_*}\left(\frac{\hbar}{i}\nabla - e_*\vec{A}\right)^2\psi = 0$$
$$-\frac{e_*}{m_*}\text{Re}\left[\psi^*\left(\frac{\hbar}{i}\nabla - e_*\vec{A}\right)\psi\right] = \vec{J}_s, \tag{2.7}$$

where α, β are phenomenological parameters. As the charge carriers are identified by Cooper pairs, the charge is given by $e_* = 2e$ and the mass is twice the electron mass $m_* = 2m_e$ [GMB64]. The first equation describes how the complex order parameter varies in presence of a magnetic vector potential $\vec{A}$. The supercurrent density $\vec{J}_s$ is associated with the order parameter ψ and the vector potential $\vec{A}$ in the second Ginzburg Landau equation. For a spatially homogeneous condensate, the superfluid density obeys the non-trivial solution

$$n_s = -\frac{\alpha}{\beta}, \tag{2.8}$$

when no magnetic field is present. The parameter β must be positive, otherwise the system is unstable, because the free energy minimizes as the superfluid density grows. Thus, $\alpha < 0$ in order to obtain a real solution. Otherwise, the superfluid density obeys the trivial solution $n_s = 0$. A purposeful choice of parameters is $\alpha \sim T - T_C$, while $\beta = const$ is fixed [HQ01]. Here T_C is the critical temperature where condensation takes place below.

The Ginzburg Landau theory predicts, in addition to the penetration depth

$$\lambda = \sqrt{\frac{mc^2}{4\pi|\psi|^2e^2}}, \tag{2.9}$$

the existence of a second parameter, the coherence length

$$\xi = \sqrt{\frac{\hbar^2}{|2m\alpha|}}, \tag{2.10}$$

which describes the length scale on which a superfluid density $n_s(\vec{r})$ changes at the boundaries of the condensate. The ratio of these two length scales defines the *Ginzburg Landau parameter*

$$\kappa = \frac{\lambda}{\xi}. \tag{2.11}$$

This parameter allows to classify two types of superconductors. A type I superconductor is classified by small penetration depth compared to the coherence length $0 < \kappa < 1/\sqrt{2}$. Thus, these materials exhibit the Meißner effect. For $\kappa > 1/\sqrt{2}$, magnetic vortices arise, when exposed to a magnetic field, allowing magnetic flux to fill into the vortices. Such materials are called type II superconductors.

2.3   Josephson effect

A quantum state has a finite probability to pass through a potential barrier even though the corresponding classical object is not in possession of enough energy to overcome the crest. This scintillating phenomenon is known as *quantum tunneling*. As this effect was well known for single electrons, it was natural to ask how Cooper pairs would face a potential barrier. In 1962, Brian Josephson proposed an approach to calculate tunneling current between two weakly linked superconductors [Jos62]. In a *Josephson junction*, two superconducting sites are separated from each other by a thin insulator of size r_0. Fig. 2.3 shows the schematic geometry of such a device. The states on the sites are given by

$$\psi_i = \sqrt{n_{si}}e^{i\phi_i}. \tag{2.12}$$

It turns out that, if the insulator is sufficiently thin, Cooper pairs are able to tunnel between the sites. Theoretically, Josephson proposed that the junction current I is given by the sine of the phase difference $\phi = \phi_1 - \phi_2$ between the two superconducting sites

$$I = I_C \sin \phi, \tag{2.13}$$

where I_C is the critical current of the junction. Josephson also proposed that an electric potential difference drives the phase difference

$$\frac{\partial \phi}{\partial t} = \frac{2e}{\hbar}V. \tag{2.14}$$

These are the two *Josephson equations*. One striking observation is that a junction current $|I| < I_C$ can flow through the barrier, event at absence of external electrical fields. This is known as the *DC Josephson effect*. At presence of a constant voltage $V = V_0$, the phase grows linear in time, due to the second Josephson relation. As a consequence, the junction current oscillates between $-I_C$ and I_C

$$I = I_C \sin\left(\frac{2e}{\hbar}V_0 t\right). \tag{2.15}$$

This is the *AC Josephson effect*. Shortly after Josephson's proposal, Anderson and Rowell confirmed the DC Josephson effect experimentally. At the absence of external voltage, they
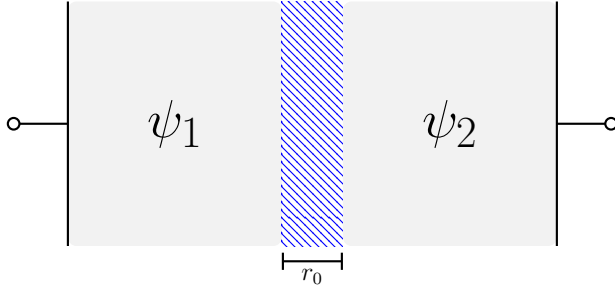
Figure 2.2: **Josephson Junction**
Two superconducting sites ψ_1, ψ_2 are coupled thru a thin insulating barrier (hatched) of size r_0. The electrical contacts of the junction are indidcated as circles.

observed current flowing between superconducting tin and lead sites, separated by a thin tin-oxide layer [AR63]. Each site had a spatial extension of $\sim 2000\text{Å}$. In 1973, Josephson was awarded with the Nobel price in physics for *the discovery of tunneling supercurrents* [Jos74].

2.4 Flux quantization

Consider a superconducting loop surrounding an empty region. The electrical current density, in presence of a magnetic field $A = \nabla \times B$, is given by the second Ginzburg Landau equation (2.7)

$$\vec{J}_s = -\frac{e_*}{m_*}\text{Re}\left[\psi^*\left(\frac{\hbar}{i}\nabla - e_*\vec{A}\right)\psi\right], \tag{2.16}$$

where $\psi = \sqrt{n_s}e^{i\phi}$ is the complex Ginzburg Landau order parameter. Assume that the loop is thick enough so that the inside is shielded from magnetic fields. Then the current density vanishes inside. If the superfluid density is homogenous inside the loop, then the second Ginzburg Landau equation yields

$$\hbar\nabla\phi = e_*A. \tag{2.17}$$

Integrating along the contour given by the loop, Stoke's theorem gives the total flux through the hole

$$\oint ds\hbar\nabla\phi = \oint dsqA = q\Phi. \tag{2.18}$$

As the order parameter is a single valued complex number, the phase must be a multiple integer of 2π when completing a full closed circuit, so the total flux is $\Phi = n\Phi_0$. In 1961, B. Deaver and W. Fairbank observed the quantization of the flux in hollow superconducting cylinders experimentally [DF61]. Also, they determined the charge to be $q = 2e$ and thus identifying the charge carriers by Cooper pairs. The *Flux quantum* is therefore

$$\Phi_0 = \frac{h}{2e}. \tag{2.19}$$

2.5   AC current response

John Drude proposed a model of moving charges through materials in which, speaking in pictures, charged particles behave like solid spheres moving through a background of oppositely charged, much heavier and localized ions. Interactions between ions and charges are described by contact interaction. In 1900, Drude proposed that such a system can be described by charges q of mass m at velocity $\vec{v}$, moving in an electric field $\vec{E}$, subject to a damping force characterized by a typical scattering time τ. The equation of motion reads [Dru00a, Dru00b]

$$m\frac{\partial \vec{v}}{\partial t} = q\vec{E} - \gamma m \vec{v} \qquad \gamma^{-1} \equiv \tau. \tag{2.20}$$

A monochromatic probing field $\vec{E}(t) = \vec{E}(\omega)e^{-i\omega t}$, and the harmonic ansatz $\vec{v}(t) = \vec{v}(\omega)e^{-i\omega t}$ for the drift velocity, solves the equation of motion

$$\vec{v}(\omega) = \frac{e\tau}{m}\frac{1}{1 - i\omega\tau}\vec{E}(\omega). \tag{2.21}$$

From the current density $\vec{J} = nq\vec{v}$, Ohm's law (2.1) leads to the conductivity response

$$\sigma = \sigma_0 \left(\frac{1}{1 + \omega^2\tau^2} + i\frac{\omega\tau}{1 + \omega^2\tau^2} \right) \qquad \sigma_0 = \frac{nq^2\tau}{m} = \frac{\omega_p^2}{4\pi}\epsilon_0\tau, \tag{2.22}$$

where the *plasma frequency* $\omega_p = \sqrt{4\pi n e^2/m}$, decribing the longitudinal oscillations of the electron gas, was introduced[Arm09]. The response of a charge having an infinite scattering time is

$$\sigma = i\frac{nq^2}{m\omega}. \tag{2.23}$$

In the London picture of a perfect superconductor, the first London equation (2.2) for a probing field at angular frequency ω yields the current density

$$\vec{J}(\omega) = \frac{n_s q^2}{m}\left(\frac{\pi}{2}\delta(\omega) + \frac{i}{\omega} \right)\vec{E}(\omega). \tag{2.24}$$

Therefore, Ohm's law identifies a pure imaginary contribution at finite angular frequencies

$$\sigma = i\frac{n_s q^2}{m\omega} \qquad \omega > 0. \tag{2.25}$$

This is the same response function as for the electron gas drifting through the conductor at absence damping forces. The real conductivity of a superconductor is zero and obtains a value at $\omega = 0$.

Chapter 3

Open quantum systems

In quantum mechanics, the Schrödinger equation generates a reversible time evolution of a closed quantum system. Real systems are subject to decoherence and dissipation which are not captured by the unitary evolution. In this chapter, irreversible dynamics are modeled by a system-plus-reservoir approach in which the system of interest is open to a reservoir. The assumptions to derive the weak Lindblad master equation are discussed followed by a numerical implementation, based on the OpenCL architecture and python3.

3.1   Statistical physics

The *density operator* represents a mixture of states defined by the probability distribution p_i

$$\rho = \sum_i p_i \, |i\rangle\langle i| \qquad \sum_i p_i = 1. \tag{3.1}$$

In thermal equilibrium at the reciprocal temperature $\beta = (k_B T)^{-1}$, the probability to find the system in a state $H\psi = E\psi$ is proportional to the Boltzmann factor $e^{-\beta E}$ and the density operator is defined by the *canonical ensemble*

$$\rho \propto \exp(-\beta H). \tag{3.2}$$

A basic operation is the *trace* of an operator O

$$\mathrm{Tr} O = \sum_i \langle i|O|i \rangle. \tag{3.3}$$

It is independent of the basis and allows to express the expectation value of O as

$$\langle O \rangle = \mathrm{Tr}(O\rho). \tag{3.4}$$

A composite state is constructed by the *tensor product*

$$\rho = \rho_A \otimes \rho_B \in \mathcal{H}_A \otimes \mathcal{H}_B. \tag{3.5}$$

An important operation over such a composite operator is the *partial trace*

$$\mathrm{Tr}_B O_A \otimes O_B = \mathrm{Tr}(O_B) O_A. \tag{3.6}$$

We now turn onto the dynamics from the perspective of the *quantum dynamical map* $\mathcal{V}$ describing a generalized evolution (super)operator. It is defined by the exponential series of $\mathcal{L}t$ where $\mathcal{L}$ is the *generator* of the evolution

$$\rho(t) = \mathcal{V}(t)\rho(0) = \exp(\mathcal{L}t)\rho(0). \tag{3.7}$$

Consider a small time step τ, then $\mathcal{V}(\tau)\rho(t) = (1 + \mathcal{L}\tau)\rho(t) + \mathcal{O}(\tau^2)$ gives the differential quotient $(\rho(t + \tau) - \rho(t))/\tau = \mathcal{L}\rho(t) + \mathcal{O}(\tau)$. Thus, the generator $\mathcal{L}$ gives the dynamics of the state $\dot{\rho} = \mathcal{L}\rho$, or $\mathcal{L} = \frac{\partial}{\partial t}$. For instance the Schrödinger equation

$$i\hbar\frac{\partial \psi}{\partial t} = H\psi$$

generates the unitary evolution of the state ψ. The corresponding time evolution operator is given by

$$U(t) = \exp(-iHt/\hbar). \tag{3.8}$$

Analogous to the quantum dynamical map, applying the time evolution operator onto a state ψ yields the state at the corresponding time $U(t)\psi(0) = \psi(t)$. Using the definition of the density operator (3.1), the quantum dynamical map is identified as

$$\mathcal{V}(t)\rho(0) = U(t)\rho(0)U^\dagger(t). \tag{3.9}$$

Differentiation yields the *Liouville von Neumann equation*

$$\mathcal{L}\rho = -\frac{i}{\hbar}[H, \rho]. \tag{3.10}$$

As U is an unitary operator, an inverse time evolution operator exists

$$U^{-1}(t) = U^\dagger(t) = U(-t) \tag{3.11}$$

Information is preserved and the evolution is reversible.

3.2 Lindblad master equation

A characterizing feature of dissipation is that entropy is not a preserved quantity. This motivates the definition of a family of quantum dynamical maps $\{\mathcal{V}(t), t > 0\}$, restricted to positive times. We now consider a system S which is coupled to an environment B. The state is given by $\rho = \rho_S \otimes \rho_B$. Following [AK07], the latter family is defined in terms of quantum dynamical maps acting on the reduced density operator ρ_S by tracing out the environment B. The environment B usually is much bigger than the reduced system S, such that excitations of the environment, induced by the reduced system, are marginal and short living compared to typical dynamical timescales of the reduced system. The *quantum dynamical semigroup* is defined as the family of quantum dynamical maps $\{\mathcal{V}(t), t > 0\}$ such that

- the semigroup condition $\mathcal{V}(t)\mathcal{V}(s) = \mathcal{V}(t + s)$ is fulfilled and

- $\text{Tr}(\mathcal{V}(t)\rho)A$ is a continuous function.

The semigroup condition implies that the semigroup group is abelian and that a coarse grained time can be constructed, i.e. $\mathcal{V}(t) = \mathcal{V}^n(t/n)$. Therefore no memory effects are involved, classifying the evolution as a *Markov chain*. In 1976, Lindblad proved that the most general generator $\mathcal{L}$ of a quantum dynamical semigroup $\mathcal{V}$ is given by the Lindblad master equation[Lin76]

$$\mathcal{L}\rho_S = -i[H, \rho_S] + \sum_\alpha \left(A_\alpha \rho_S A_\alpha^\dagger - \frac{1}{2}\{A_\alpha^\dagger A_\alpha, \rho_S\} \right). \tag{3.12}$$

The first term is the von-Neumann equation describing the unitary dynamics of the open system while the sum term describes effective irreversible dynamics, induced by the environment.

3.3   Markovian master equation

A *Markov process* makes predictions about a future state, based on the current state without including memory effects. Following [Car02] we want to take a closer look on the assumptions and steps which are required to map from the full unitary dynamics of the closed system to the markovian dynamics of the reduced system.

Consider the Hamiltonian of the open system S coupled to an environment B

$$H = H_S \otimes \mathrm{Id}_B + \mathrm{Id}_S \otimes H_B + \alpha V, \tag{3.13}$$

where H_S is the Hamiltonian of the open system and H_B is the Hamiltonian of the environment. The interaction Hamiltonian αV describes the coupling between the open system and the exterior. In the *Born approximation*, the coupling is assumed to be small $\alpha \ll 1$ as well as effects from the open system on the environment. At initial time, the state is assumed to be a product state of the form

$$\rho(0) = \rho_S(0) \otimes \rho_B(0), \tag{3.14}$$

neglecting correlations between the system and the bath at initial time. This is a valid approximation as the coupling is assumed to be small. In general, the system tends towards the true equilibrium state $\mathrm{Tr}_B(H_S \otimes \mathrm{Id}_B + \mathrm{Id}_S \otimes H_B + \alpha V)$ even though it was setup in an uncorrelated equilibrium state. This transient phenomenon is known as *initial sweeping*[Tan14]. As the Hamiltonians $H_S \otimes \mathrm{Id}_B$ and $\mathrm{Id}_S \otimes H_B$ describe the unitary evolution of ρ_S and ρ_B, only the coupling αV is included into the upcoming steps. Given the initial state $\rho(0)$, the equation of motion at time t, in the interaction picture, is given by the von-Neumann equation

$$\frac{\partial \rho(t)}{\partial t} = -i\alpha \big[V(t), \rho(0)\big] - \frac{\alpha^2}{\hbar^2} \int_0^t ds \big[V(t), \big[V(s), \rho(s)\big]\big]. \tag{3.15}$$

Reinserting, an expansion in powers of α is obtained. Higher order terms $\mathcal{O}(\alpha^3)$ are truncated due to weak coupling. As $-\mathrm{Tr}_B\big[V(t), \rho(0)\big]\mathrm{Id}_S$ is an arbitrary energy shift, it has no effect on the dynamics and will be ignored in the following steps. The environmental degrees of freedom are traced out

$$\frac{\partial \rho(t)}{\partial t} = -\frac{\alpha^2}{\hbar^2} \int_0^t ds \mathrm{Tr}_B\big[V(t), \big[V(s), \rho(s)\big]\big]. \tag{3.16}$$

Assuming that bath excitations are not resolved by the coarse grained time axis corresponding to the Markov chain, the state can be approximated as[RH12]

$$\rho(t) \to \rho_S(t) \otimes \rho_B, \tag{3.17}$$

where $\rho_B(t) \equiv \rho_B = $ const. Furthermore, the *Markov approximation* replaces the state at retarded time by a state at local time $\rho_S(s) \to \rho_S(t)$, which leads to a separation of time scales

$$\frac{\partial \rho(t)}{\partial t} = -\frac{\alpha^2}{\hbar^2} \int_0^t ds \, \mathrm{Tr}_B \big[V(t), \big[V(s), \rho(t) \big] \big]. \tag{3.18}$$

This is the *Redfield equation*, local in time, but depending on the explicit choice of the initial conditions. If one further assumes that bath correlations decay sufficiently fast, compared to the typical system relaxation time $\tau_B \ll \tau_R$, then the integral kernel vanishes for $s \gg \tau_B$, allowing to set the upper bound of the integral to infinity. Substituting $s \to t - s$ does not change the integral bounds and gives the *Markov master equation*

$$\frac{\partial \rho(t)}{\partial t} = -\frac{\alpha^2}{\hbar^2} \int_0^\infty ds \, \mathrm{Tr}_B \big[V(t), \big[V(t - s), \rho(t) \big] \big], \tag{3.19}$$

which does not depend on the initial conditions as the interaction Hamiltonian $V(t - s)$ is integrated from t to $-\infty$.

3.4 Weak coupling master equation

In general, the Markov master equation (3.19) does not generate a semigroup acting on the reduced system [RH12]. In this section, the interaction Hamiltonian is written in the most general form, allowing to define the interaction Hamiltonian in terms of eigenoperators of the reduced system. This representation allows to perform the secular approximation leading to the Lindblad form (3.12). Consider the generic interaction Hamiltonian

$$V = \sum_\alpha A_\alpha \otimes B_\alpha, \tag{3.20}$$

where $A_\alpha \in \mathcal{H}_S$ are hermitian operators of the system S, and $B_\alpha \in \mathcal{H}_B$ are hermitian operators of the bath B. The spectrum of the open system $H_S |s\rangle = \epsilon_s |s\rangle$ defines a representation of the coupling operators in terms of the energy differences between energy states

$$A_\alpha = \sum_\omega A_\alpha(\omega). \tag{3.21}$$

The transition operators explicitly can be represented as

$$A_\alpha(\omega) = \sum_{\omega_{ab}} \delta(\omega_{ab} - \omega) A_\alpha^{ab} |a\rangle\langle b| \qquad \hbar\omega_{ab} = \epsilon_b - \epsilon_a \qquad A_\alpha^{ab} = \langle a | A_\alpha | b \rangle. \tag{3.22}$$

The decay channels are weighted by the matrix elements A_α^{ab}. It follows from

$$H A_\alpha(\omega) |c\rangle = \sum_{\omega_{ac}} \epsilon_a A_\alpha^{ac} \delta(\omega_{ac} - \omega) |a\rangle$$

$$A_\alpha(\omega) H |c\rangle = \sum_{\omega_{ac}} \epsilon_c A_\alpha^{ac} \delta(\omega_{ac} - \omega) |a\rangle, \tag{3.23}$$

that the transition operator $A_\alpha(\omega)$ represents a decay between states having an energy difference $\hbar\omega$, namely

$$[H_S, A_\alpha(\omega)] = -\hbar\omega A_\alpha(\omega), \tag{3.24}$$

therefore

$$A_\alpha(-\omega) = A_\alpha^\dagger(\omega). \tag{3.25}$$

To illuminate the meaning of the transition operators $A_\alpha(\omega)$, we want to take a closer look on the matrix representation. Note that the transition operators are sparse in the energy base $\mathcal{B}$, which will be the main ansatz for numerical optimizations later on. For instance, if a transition frequency belongs uniquely between two states $|a\rangle \to |b\rangle$, then $(M_\mathcal{B}^{-1} A(\omega) M_\mathcal{B})_{ij} = A^{ij}\delta_{ia}\delta_{jb}$. Another example is the harmonic oscillator $\hbar\omega a^\dagger a$, where the transition operators are identified by powers of the annihilation operator $A(n\omega) = a^n$.

Resuming the derivation, using Baker Hausdorf's identity, the transition operators rotate in the interaction picture

$$e^{iH_s t/\hbar} A_\alpha(\omega) e^{-iH_s t/\hbar} = e^{-i\omega t} A_\alpha(\omega)$$

In the rotating frame, the interaction Hamiltonian can now be written as

$$V(t) = \sum_{\alpha\omega} e^{-i\omega t/\hbar} A_\alpha(\omega) \otimes B_\alpha(t). \tag{3.26}$$

Tracing out the environment and using basic properties of the trace, the Markov master equation (3.19) obtains a form in which rotating terms manifest

$$\frac{\partial \rho_S(t)}{\partial t} = -\sum_{\alpha\omega}\sum_{\beta\omega'} e^{i(\omega'-\omega)t/\hbar} \Gamma_{\alpha\beta}(\omega) \left[A_\alpha^\dagger(\omega') A_\beta(\omega)\rho(t) - A_\beta(\omega)\rho(t) A_\alpha^\dagger(\omega') \right] + \text{h.c}, \tag{3.27}$$

where the half sided Fourier transform over the two time correlation function of the bath operators defines the *spectral correlation tensor*

$$\Gamma_{\alpha\beta}(\omega) = \frac{1}{\hbar^2} \int_0^\infty ds\, e^{i\omega s} \big\langle B_\alpha(t) B_\beta(t-s) \big\rangle. \tag{3.28}$$

Assuming that the relaxation time τ_R of the open system does not resolve the secular oscillations, i.e. $|\omega'-\omega|^{-1} \ll \tau_R$, then the secular terms average out and the approximation $e^{i(\omega'-\omega)t} \to \delta(\omega-\omega')$ becomes valid. More precisely, this is an application of the *Riemann-Lebesgue-lemma*[RH12] which states that the spectrum of an integrable function vanishes for infinite frequencies

$$\lim_{\omega\to\infty} \int dt\, e^{i\omega t} f(t) = 0. \tag{3.29}$$

The latter is the called *secular approximation* and the resulting master equation is

$$\frac{\partial \rho_S(t)}{\partial t} = \sum_{\alpha\beta\omega} \Gamma_{\alpha\beta}(\omega) \left[A_\beta(\omega)\rho(t)A_\alpha^\dagger(\omega') - A_\alpha^\dagger(\omega')A_\beta(\omega)\rho(t) \right] + \text{h.c.} \tag{3.30}$$

The real part of the spectral correlation tensor $\Gamma_{\alpha\beta}(\omega) = \gamma_{\alpha\beta}(\omega)/2 + iS_{\alpha\beta}(\omega)$ specifies the rate of non-unitary dynamics $\mathcal{D}\rho_S$, while the imaginary part contributes to the unitary generator, leading to a renormalization of the spectrum, also known as the *Lamb-shift*

$$H_{\text{LS}} = \sum_{\alpha\beta\omega} S_{\alpha\beta}(\omega)A_\alpha^\dagger(\omega)A_\beta(\omega). \tag{3.31}$$

Relativistic effects must be taken into account in order to evaluate the ultraviolet divergent integrant of $S_{\alpha\beta}(\omega)$[Sch08]. We assume the Lamb-shift contributions to be small and set $S_{\alpha\beta}(\omega) = 0$ for the upcoming discussions. The dissipator of the *weak coupling master equation* is [BP02, Wei99]

$$\mathcal{D}\rho_S = \sum_{\alpha\beta\omega} \gamma_{\alpha\beta}(\omega) \left[A_\beta(\omega)\rho_S A_\alpha^\dagger(\omega) - \frac{1}{2}\left\{ A_\beta(\omega)A_\alpha^\dagger(\omega), \rho_S \right\} \right]$$

$$\gamma_{\alpha\beta}(\omega) = \frac{1}{\hbar^2} \int ds e^{i\omega s} \langle B_\alpha(s)B_\beta(0) \rangle. \tag{3.32}$$

Here it was assumed that the bath is in a stationary state.

3.5 Optical master equation

The Hamiltonian of the quantized electromagnetic field is [Sch07]

$$H = \sum_{k\lambda} \hbar\omega_k a_{k\lambda}^\dagger a_{k\lambda}, \tag{3.33}$$

where $a_{k\lambda}$ is the annihilation operator of the mode k with polarization λ. The annihilation operators obey the canonical commutation relation $[a_{k\lambda}, a_{l\sigma}^\dagger] = \delta_{kl}\delta_{\lambda\sigma}$ and the dispersion relation $\hbar\omega_k = ck$ with $k = |\vec{k}|$. The polarization vectors and the mode form an orthogonal basis

$$\vec{k} \cdot \vec{e}_{\lambda k} = 0 \qquad \vec{e}_{\lambda k} \cdot \vec{e}_{\sigma k} = \delta_{\lambda\sigma} \qquad \sum_\lambda e_{\lambda k}^i e_{\lambda k}^j = \delta_{ij} - \frac{k_i k_j}{k^2}. \tag{3.34}$$

In the interaction picture, the electric field operator can be written as

$$E_j(t) = i \sum_{k\lambda} \sqrt{\frac{2\pi\hbar\omega_k}{\epsilon_0 V}} e_{\lambda k}^j \left(a_k e^{ikx - i\omega_k t} - a_k^\dagger e^{-ikx + i\omega_k t} \right) \tag{3.35}$$

. We will consider the bath to be in thermal equilibrium

$$\rho = \prod_{k\lambda}(1 - \exp(-\beta\hbar\omega_k))\exp\left(-\beta\hbar\omega_k a_{k\lambda}^\dagger a_{k\lambda}\right) \tag{3.36}$$

, where we have used the geometric series to evaluate the partition sum

$$Z_\lambda = \prod_k \operatorname{Tr}\exp\left(-\beta\hbar\omega_k a_{k\lambda}^\dagger a_{k\lambda}\right) = \prod_k \sum_{k_l}\exp(-\beta\hbar\omega_k k_l) = \prod_k \frac{1}{1 - \exp(-\beta\hbar\omega_k k_l)}. \tag{3.37}$$

A single mode obeys the mean occupation number

$$N(\omega) = \operatorname{Tr}(a^\dagger a\rho) = \frac{1}{e^{\beta\hbar\omega} - 1} \tag{3.38}$$

and the correlations of the annihilation operators evaluate to

$$\begin{aligned}
\langle a_k^\dagger a_l\rangle &= \delta_{kl}N(\omega_k)\\
\langle a_k a_l^\dagger\rangle &= \langle[a_k, a_l^\dagger] + a_k^\dagger a_l\rangle = \delta_{kl}(1 + N(\omega_k))\\
\langle a_k a_l\rangle &= \langle a_k^\dagger a_l^\dagger\rangle = 0.
\end{aligned} \tag{3.39}$$

With (3.39) the correlation of the electromagnetic field operator (3.35) gets

$$\left\langle E_i(s)E_j(0)\right\rangle_B = \frac{2\pi\hbar}{V}\sum_k \omega_k\left(\sum_\lambda e_\lambda^i(k)e_\lambda^j(k)\right)\left[N(\omega_k)e^{i\omega_k s} + (1 + N(\omega_k))e^{-i\omega_k s}\right]. \tag{3.40}$$

Going into the continuum limit and using the polarization structure of the electromagnetic field (3.34), one obtains

$$\frac{2\pi\hbar}{V}\sum_k \omega_k\left(\sum_\lambda e_\lambda^i(k)e_\lambda^j(k)\right) = \frac{\hbar}{(2\pi)^2 c^3}\int_0^\infty d\omega\omega_k^3\int d\Omega\left(\delta_{ij} - \frac{k_i k_j}{|k|^2}\right). \tag{3.41}$$

The integration over the solid angle has the solution

$$\int d\Omega\left(\delta_{ij} - \frac{k_i k_j}{|k|^2}\right) = \frac{8\pi}{3}\delta_{ij}, \tag{3.42}$$

so the spectral weight (3.32) evaluates to

$$\gamma_{ij}(\omega) = \frac{2\delta_{ij}}{3\pi\hbar c^3}\int ds\int_0^\infty d\omega_k\omega_k^3\left[N(\omega_k)e^{i(\omega_k+\omega)s} + (1 + N(\omega_k))e^{-i(\omega_k-\omega)s}\right]. \tag{3.43}$$

Because

$$\int ds\, e^{i\omega s} = 2\pi\delta(\omega), \tag{3.44}$$

the spectral weight of the dissipator $\mathcal{D}A(\omega)$ is

$$\gamma(\omega) = \frac{4\omega^3}{3\hbar\epsilon_0 c^3}(1 + N(\omega)) \tag{3.45}$$

This is a well known result from quantum optics, also known as *Einstein coefficients*. The spectral weight $\gamma(\omega) \sim \omega^3(1 + N(\omega))$ describes spontaneous and stimulated photon emission while $\gamma(\omega) \sim \omega^3 N(\omega)$ describes photon absorption. Evaluating $\gamma(\omega)/\gamma(-\omega) \sim e^{\beta\hbar\omega}$ yields the thermodynamic equilibrium ratio of canonical ensemble occupation probabilities corresponding to the involved states. Note that the spontaneous emission has its origin in the canonical commutation relation and thus is a quantum mechanical effect.

3.6   Numerical implementation

The dynamics of the density operator, having dimension $d = \dim\mathcal{H}$, is described by $d(d + 1)/2$ ordinary differential equations $\frac{\partial\rho_{ij}}{\partial t}$. The unitary evolution is generated by the matrix products $H\rho$ and ρH, while the irreversible part contains products of the form $A^\dagger A\rho$, $\rho A^\dagger A$ and $A\rho A^\dagger$. In general, this implies that the arithmetic evaluation of $\frac{\partial\rho_{ij}}{\partial t}$ has $\mathcal{O}(ld^2)$, where l is the number of dissipators $\mathcal{D}A$. However, in the weak coupling master equation (3.32), the operators $A(\omega)$ describe transitions between states as they lower the energy by $\hbar\omega$ and thus, they are sparse in the energy basis. For instance, having $d = 5$ states, the transition from $H\,|3\rangle = \epsilon\,|3\rangle$ into the degenerate states $H\,|2\rangle = \epsilon'\,|2\rangle$ and $H\,|1\rangle = \epsilon'\,|1\rangle$ takes form

$$A((\epsilon - \epsilon')/\hbar) \sim \begin{pmatrix} 0 & 0 & a_{13} & 0 & 0 \\ 0 & 0 & a_{23} & 0 & 0 \\ 0 & 0 & 0 & 0 & 0 \\ 0 & 0 & 0 & 0 & 0 \\ 0 & 0 & 0 & 0 & 0 \end{pmatrix}. \tag{3.46}$$

This motivates a numerical implementation, which exploits the sparseness of $A(\omega)$ in order to gain computational performance by optimizing the arithmetic evaluation of the matrix products. This section documents, how the weak coupling master equation (3.32) is implemented within the OpenCL[1] architecture.

Work-Item representation

Each equation $\frac{\partial\rho_{xy}}{\partial t}$ is computed by a work-item[2] (x, y), following the instructions given by the matrix element $\langle x|\dot\rho|y\rangle$ where $|x\rangle, |y\rangle$ are eigenstates of H. The von Neumann dynamics are governed by

$$\langle x|[H, \rho]|y\rangle = \sum_j \left(H_{xj}\rho_{jy} - \rho_{xj}H_{jy}\right). \tag{3.47}$$

The following representation of the transition operator (3.22) is convenient within this section

$$A(\omega) = \sum_{\omega_{ij}} \delta(\omega_{ij} - \omega)A_{ij}\,|i\rangle\langle j| \equiv \sum_{\omega[ij]} |i\rangle\langle j| \tag{3.48}$$

$$A^\dagger(\omega) = \sum_{\omega_{ij}} \delta(\omega_{ij} - \omega)A^*_{ij*}\,|j\rangle\langle i| \equiv \sum_{\omega[ij]^*} |j\rangle\langle i|. \tag{3.49}$$

An explicit representation of the operators is given in Appendix A.

---

[1]khronos.org/registry/OpenCL/specs/opencl-1.2.pdf

[2]OpenCL1.2 specification: "One of a collection of parallel executions of a kernel invoked on a device by a command. A work-item is executed by one or more processing elements as part of a work-group executing on a compute unit. [...]". The corresponding work-group represents the density operator.

The Rate Tensor

The work-item representations give rise to the computational instructions for each work-item (x, y). Note, that the anti-commutator terms have a free running index, as they collect contributions from the same row x and column y. It is purposeful to fix the source matrix elements ρ_{ab} (see Appendix A), in order to get a representation, which collects all contributions from a matrix element ρ_{ab} into the work item ρ_{xy}. This defines the *rate tensor*

$$R_{xy}^{ab} \equiv \sum_{\omega} \gamma(\omega) \left[\sum_{\omega[xa]} \sum_{\omega[yb]^*} -\frac{1}{2} \sum_{\omega[xj]} \sum_{\omega[aj]^*} \delta_{by} - \frac{1}{2} \sum_{\omega[bj]} \sum_{\omega[yj]^*} \delta_{xa} \right]. \tag{3.50}$$

The first term represents the flow into ρ_{xy} while the second (the third) represents a dissipative flow out of the matrix element ρ_{xy} onto the same column (row). With the observation that

$$\sum_{ab} \sum_{\omega[xa]} \sum_{\omega[yb]^*} \rho_{ab} = \sum_{\omega[xi]} \sum_{\omega[yj]^*} \rho_{ij} \qquad \sum_{ab} \sum_{\omega[xj]} \sum_{\omega[aj]^*} \delta_{by}\rho_{ab} = \sum_{\omega[xj]} \sum_{\omega[ij]^*} \rho_{iy}, \tag{3.51}$$

it is easy to proof that (3.50) describes the full dissipator

$$\sum_{ab} R_{xy}^{ab} \rho_{ab} = (\mathcal{D}\rho)_{xy}. \tag{3.52}$$

This representation is the basis for the upcoming implementation.

Implementation

The Lindblad equation is an ordinary differential equation (ODE). Runge Kutta (RK) methods provide a simple schema to integrate an ODE in time. On a coarse time axis, the sequence of states is defined as

$$\rho_{n+1} = \rho_n + \Delta t \sum_{i=1}^{s} b_i k_i. \tag{3.53}$$

The explicit 3rd order Runge Kutta method (the error is of order $\mathcal{O}(4)$) is used where $b_1 = b_3 = 1/6$, $b_2 = 2/3$ and the Butcher scheme is [PTVF07]

$$\begin{aligned}
k_1 &= \mathcal{L}[\rho_n](t_n) \\
k_2 &= \mathcal{L}[\rho_n + \Delta t/2k_1](t_n + \Delta t/2) \\
k_3 &= \mathcal{L}[\rho_n - \Delta t(k_1 - 2k_2)](t_n + \Delta t).
\end{aligned} \tag{3.54}$$

From the rate tensor (3.52) we define the following iterative protocol

$$\langle x|\mathcal{D}\rho|y\rangle = \sum_{ab} R_{xy}^{ab} \rho_{ab}. \tag{3.55}$$

On pre-compile stage, for each work item (x, y), the rate tensor elements R_{xy}^{ab} are computed for all (a, b) and we define the set of non-zero contributions as

$$\mathcal{J}_{xy} = \{(a, b) : |R_{xy}^{ab}| \neq 0\}. \tag{3.56}$$

The irreversible contribution into $\dot{\rho}_{xy}$ is now a single sum with a maximum of $|\mathcal{J}_{xy}| \leq d(d+1)/2$ summands

$$(\mathcal{D}\rho)_{xy} = \sum_{(a,b)\in\mathcal{J}_{xy}} R_{xy}^{ab}\rho_{ab}. \tag{3.57}$$

Recall that the raw arithmetic evaluation has $\mathcal{O}(ld^2)$. The precompiler generates $\max_{xy}|\mathcal{J}_{xy}|$ lines of code representing the latter sum. As the unitary part of the evolution may contain time dependent terms, it does not fit into the scheme above and is therefore implemented as (3.47) separately. The library supports time dependent Hamiltonians of form

$$H(t) = \sum_i H_i f_i(t), \tag{3.58}$$

by uploading the time independent Hamiltonians H_i into the buffer and rendering $f_i(t)$ into the kernel source at pre-compile stage. The version implemented for this thesis supports one coupling term in the coupling Hamiltonian (3.20). This representation benefits from the linear properties of the equation by summing several contributions from a matrix element into a single weight. In fact, most of the savings arise from the sparseness of the transition operators. The systems analyzed in this thesis will usually have $d = 15$, $l \sim 90$ transitions. Due to the above optimization, circa $\max_{xy}|\mathcal{J}_{xy}| \sim 10$ summands are required in (3.57) while the pure arithmetic implementation would require $ld^2 \sim 2 \times 10^4$ operations per work item in order to evaluate the matrix products.

After calculating a sequence ρ_{t_i} on the GPU, the CPU starts post-processing the sequence, i.e. evaluate expectations values. Simultaneously, the GPU begins evolving the next sequence so that both computing units work aside. As a strategy to ensure the correctness of the library, a reference implementation, based on QuTip [JNN12, JNN13], is implemented using the full representation of the transition operators $A(\omega)$. Using pytest[2], several scenarios are tested, comparing the result of the optimized OpenCL kernel against the unoptimized QuTip kernel by asserting equality in terms of floating point precision. The full implementation is available on the author's github page[3]. Appendix B provides a minimal library usage code example.

---

[2]docs.pytest.org/en/latest/
[3]github.com/keksnicoh/qoptical

Chapter 4

Quantum Josephson junction

4.1   Quantized Josephson junction

In this section, the basic Hamiltonian used within this thesis is introduced. The geometry of a Josephson Junction can be thought of as a capacitor. The capacitance C describes the amount of charge Q stored on the electrodes when a voltage V is present

$$Q = CV. \tag{4.1}$$

The electrical current I is the rate at which charge Q flows

$$I = \frac{\partial Q}{\partial t} = C\frac{\partial V}{\partial t}. \tag{4.2}$$

The total current is composed by an external current I_e and the junction current I_j. Using the first Josephson relation (2.13) the total amount of current is

$$I = I_c \sin\phi - I_e. \tag{4.3}$$

The second Josephson equation (2.14) evaluates the equation of motion of the phase

$$\frac{\partial^2 \phi}{\partial t^2} = -\frac{2\pi}{\Phi_0}\frac{\partial V}{\partial t} = -\frac{2\pi}{\Phi_0}\frac{I}{C}, \tag{4.4}$$

which is the Euler-Lagrange equation of the Lagrange function

$$L = \frac{C}{2}\left(\frac{\Phi_0}{2\pi}\right)^2 \dot{\phi}^2 + \frac{\Phi_0}{2\pi}\left(I_c \cos\phi + I_e\phi\right). \tag{4.5}$$

At absence of an external current, the latter is the Lagrangian of the pendulum. In the harmonic limit, the linear pendulum frequency is given by

$$\omega_0 = \sqrt{\frac{2\pi}{\Phi_0}\frac{I_c}{C}}. \tag{4.6}$$

The canonical conjugate to the phase ϕ is

$$\chi = \frac{\partial L}{\partial \dot{\phi}} = \left(\frac{\Phi_0}{2\pi}\right)^2 C\dot{\phi}. \tag{4.7}$$

Note that $\chi = -\hbar Q/e_*$ and thus quantifies the charge imbalance between the two sites of the junction. The Legendre transformation gives the Hamiltonian

$$H = \frac{1}{2C}\left(\frac{2\pi}{\Phi_0}\right)^2 \chi^2 - \frac{\Phi_0}{2\pi}\left(I_c \cos\phi + I_e\phi\right). \tag{4.8}$$

The system is quantized by replacing the conjugate variables by operators and imposing the canonical commutation relation [NT08]

$$[\phi, \chi] = i\hbar, \tag{4.9}$$

and therefore

$$\chi = \frac{\hbar}{i} \frac{\partial}{\partial \phi}. \tag{4.10}$$

By defining the *charge operator*

$$\delta n = \frac{\chi}{\hbar},$$

the Hamiltonian (4.8) gets

$$H = \frac{E_c}{2} \delta n^2 - J_0 \cos(\phi) + \frac{\Phi_0}{2\pi} I_e \phi, \tag{4.11}$$

where the characterizing energy scales, the *charge energy* and the *Josephson energy*, are introduced

$$E_c = \left(\frac{2\pi\hbar}{\Phi_0}\right)^2 \frac{1}{C} \qquad J_0 = \frac{\Phi_0}{2\pi} I_c. \tag{4.12}$$

The linearized pendulum frequency can now be written as $\hbar\omega_0 = \sqrt{E_C J_0}$. From the Heisenberg equation of motion for the phase difference $\hbar\dot{\phi} = i[H, \phi]$ the quantum equivalent of the second Josephson relation (2.14) is

$$V = \frac{E_C}{e_*} \delta n. \tag{4.13}$$

Without an external current, the Schrödinger equation corresponding to (4.11) is a Mathieu equation [BB05]

$$-\frac{E_c}{2} \frac{d\psi^2}{d\phi^2} \psi - J_0 \cos(\phi)\psi = E\psi. \tag{4.14}$$

Turning on the details of the spectrum we want to discuss some of its features. States having an energy below the Josephson energy are considered bound, while the others, able to overcome the barrier, are considered unbound. In the pendulum analogue, bound states oscillate around $\phi = 0$, while unbound states do not change direction as they are able to overcome the phase $\phi = \pi$ where the potential energy maximized. Fig. 4.1 shows the spectrum of the system. Compared to the classical pendulum, the phase is described by a probability distribution $|\psi(\phi)|^2$. Classically, at the turning points, the phase slows down and changes direction eventually, which is manifest in the quantum picture as a high probability $|\psi(\phi)|^2$ near the turning point ($\dot{\phi} = 0$). States having just enough energy to overcome the potential have a high probability at $\phi = \pi$ as $\dot{\phi}(\phi)$ gets close to zero. Quantum tunneling allows passing $\phi = \pi$ even though the energy is below the Josephson energy.
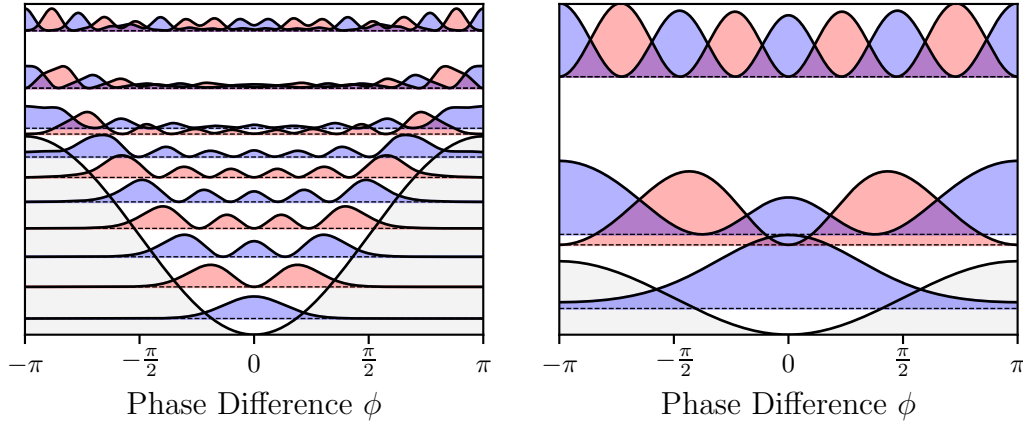
Figure 4.1: **Spectrum of** H_0
The probability $|\psi_i(\phi)|^2$ is depicted such that it is shifted to the corresponding eigenenergy E_i. The parity is indicated by blue / red faces. **left**: Josephson regime, the harmonic limit becomes eminent. **right**: Charge regime, free rotor states dominate the spectrum.

In the upcoming discussions, it is useful to quantify the ratio between the characterizing energy scales of the junction

$$\eta = \frac{E_c}{J_0}. \tag{4.15}$$

Ratios $\eta > 1$ are referred to be in the *charge regime*. In the charge limit $\eta = \infty$ the spectrum is given by the free modes $e^{ik\phi}$ having an energy $E_c k^2/2$. Thus, the free rotor states are degenerate. In the opposite limit $\eta \to 0$, which will be referred as the *Josephson regime*, the spectrum is not degenerate. The ground state can be approximated by the ground state of the harmonic oscillator. As the energy grows, the energy difference between the states shrink as they eventually become unbound degenerate.
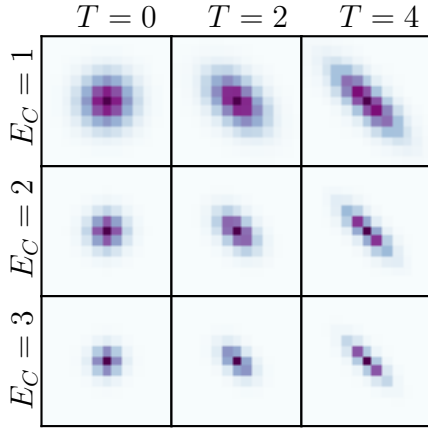
Figure 4.2: **Thermal density operator**
Absolute value representation of ρ_{eq} in free rotor basis.
The $k = 0$ mode is centered. All junctions have a linear
frequency of $\omega_0 = 3$ (thus $J_0 = \omega_0^2/E_c$) and the units
are dropped. As the charging energy becomes dominant,
the coherence between the modes decreases.

4.2   Dissipative model

In this section we extend the Hamiltonian (4.11) by an electromagnetic field and a coupling
Hamiltonian. As an ansatz, consider the junction to form a dipole when a charge imbalance
between the two sites occur. Using the charge operator, a dipole normal to the insulating
barrier, is defined as

$$d = e_* r_0 \delta n, \tag{4.16}$$

where r_0 is the width of the barrier. In an electrical field, a dipole has the potential energy

$$V = -dE. \tag{4.17}$$

In the Schrödinger picture, using (4.11) and (3.33), the Hamiltonian of the Josephson junc-
tion within an electrical field is

$$
\begin{aligned}
H &= \left(\frac{E_c}{2} \delta n^2 - J_0 \cos(\phi) + \frac{\Phi_0}{2\pi} I \phi \right) \otimes \mathrm{Id}_B \\
&\quad + \mathrm{Id}_S \otimes \sum_{k\lambda} \hbar \omega_k a_{k\lambda}^\dagger a_{k\lambda} \\
&\quad + r_0 e_* \delta n \otimes i \sum_{k\lambda} \sqrt{\frac{2\pi\hbar\omega_k}{\epsilon_0 V}} e_{\lambda k} \left(a_k e^{ikx} - a_k^\dagger e^{-ikx} \right).
\end{aligned}
\tag{4.18}
$$

In the weak coupling limit (3.32), a quantum dynamical semigroup of a system coupled thru
a dipole to the electromagnetic field is generated by the following Lindblad master equation

$$\mathcal{L}\rho = -\frac{i}{\hbar} \left[H_S, \rho \right] + \sum_\omega \gamma(\omega) \mathcal{D}\delta n(\omega) \rho, \tag{4.19}$$

with the transition operators

$$\delta n(\omega) = \sum_{\omega_{ab}} \delta(\omega_{ab} - \omega) \langle a | \delta n | b \rangle \, | a \rangle\langle b |, \tag{4.20}$$

and using (3.45) the dissipation

$$\gamma(\omega) = \kappa\omega^3(1 + N(\omega)), \tag{4.21}$$

where we have defined

$$\kappa = \frac{4r_0^2 e_*^2}{3\hbar\epsilon_0 c^3}. \tag{4.22}$$

Note that $[\kappa] = s^2$ and thus $[\gamma(\omega)] = s^{-1}$. Each Lindblad term corresponds to the emission $\gamma(|\omega|)\mathcal{D}A(|\omega|)$ of photons or absorption of photons $\gamma(-|\omega|)\mathcal{D}A(-|\omega|)$. Figure 4.3 gives an impression of the Josephson junction coupled to the electromagnetic field.

Due to symmetry, $\langle a|\delta n|b\rangle = 0$ for states $|a\rangle$ and $|b\rangle$ of opposite parity, a selection rule is defined. In the continuum, the states are degenerate and thus the operators $A(\omega)$ contain two projections between the four involved states (see Fig. 4.4), leading to coherence processes from the jump terms $A^\dagger(\omega)\rho A(\omega)$.

The emission and absorption processes of each dissipation channel are characterized by specific damping rates $\gamma(\omega)$. We define the characterizing damping rate of the junction in terms of the spontaneous emission rate of the plasma mode

$$\tilde{\gamma} = (\kappa\omega_{\mathrm{Jp}}^2)\omega_{\mathrm{Jp}}. \tag{4.23}$$

4.3 Matrix expansion

A finite dimensional representation of the operators is of interest. We expand the Hamiltonian in $\dim\mathcal{H}$ modes $e^{ik\phi}$. Recall that the inner product is

$$\langle f|g\rangle = \frac{1}{2\pi}\int d\phi f^* g. \tag{4.24}$$

The matrix elements of the charge operator compute to

$$(\delta n)_{lk} = \frac{-i}{2\pi}\int d\phi e^{-il\phi}\partial_\phi e^{ik\phi} = \delta_{lk}k. \tag{4.25}$$
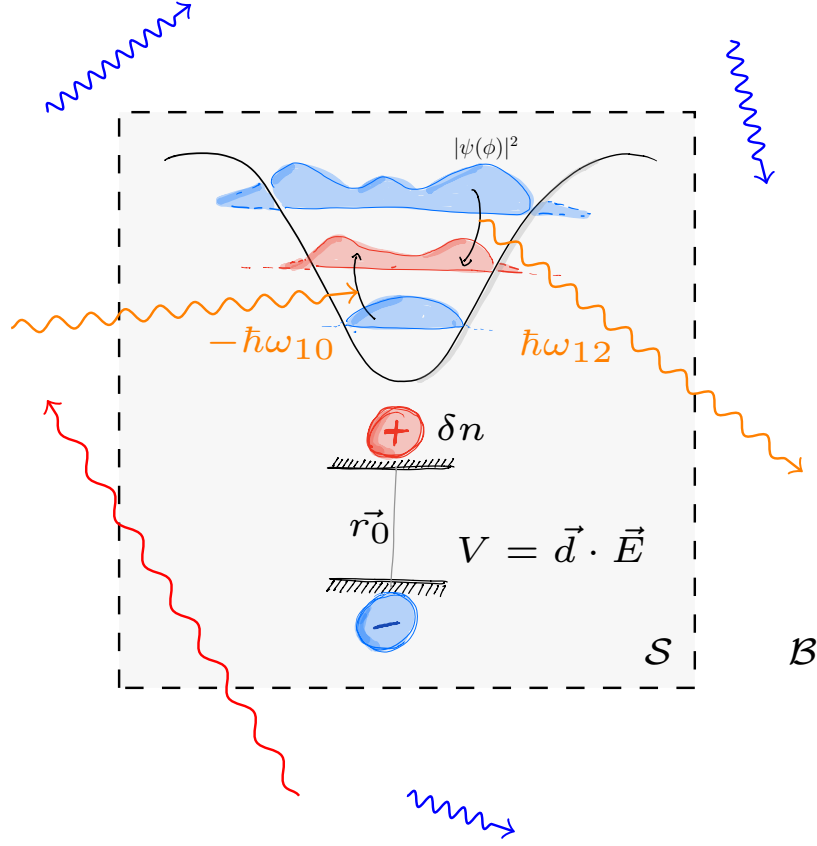
From a single mode

$$(e^{im\phi})_{lk} = \frac{1}{2\pi}\int d\phi e^{-il\phi}e^{i(k+m)\phi} = \delta_{l(k+m)}, \tag{4.26}$$
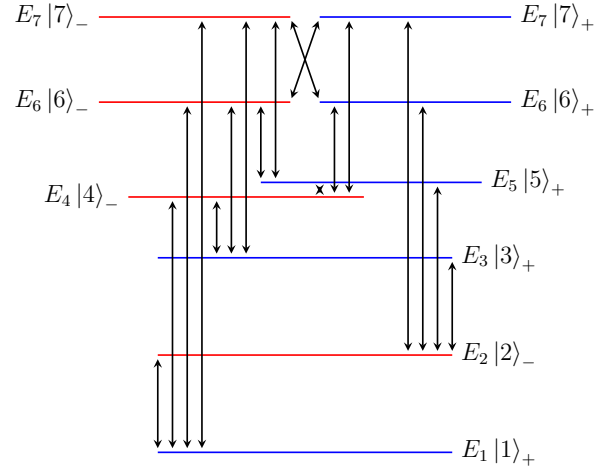
the trigonometric functions are computed to be

$$2(\cos\phi)_{ik} = \delta_{i(k+1)} + \delta_{(i+1)k}$$
$$2i(\sin\phi)_{ik} = \delta_{i(k+1)} - \delta_{(i+1)k} \tag{4.27}$$
$$4(\sin^2\phi)_{ik} = 2\delta_{ik} - \delta_{i(k+2)} - \delta_{(i+2)k}.$$

The phase ϕ has $\phi_{ll} = \pi/2$ and the off diagonal elements are

$$\phi_{lk} = \frac{i(-1)^{k-l+1}}{k-l}. \tag{4.28}$$

Figure 4.3: **Josephson junction coupled to a bath of photons**
Sketch of the dissipative model. The junction absorbs and emits photons from the electromagnetic field thru dipole coupling.

Figure 4.4: **Dissipation channels**
Spectrum of H_0. Transitions having a finite dipole transition matrix element are depicted as arrows. The parity of the states is indicated by blue (+) and red (-) color.

4.4   Conductivity

In the *two fluid model* [Tin96], the electron density divides into two parts: the density of normal electrons n_n and of condensed electrons n_s

$$n = n_n + n_s. \tag{4.29}$$

Both species are assumed to behave effectively like Drude gases (2.20) characterized by typical scattering times τ_n, τ_s. At zero temperature the junction is governed by Cooper pairs $n = n_s$. In the London picture the Cooper pairs move freely $\tau_s = \infty$, leading to a divergence of the imaginary conductivity. The slope is proportional to the Josephson energy which quantifies the superconductivity of the junction. Okamoto et al. established a definition of an effective Josephson energy as $J_{\mathrm{eff}} \propto \lim_{\omega \to \infty} \mathrm{Im}\omega\sigma(\omega)$ [OCM16b, OHCM17, OCM16a, Hom18]. This integrates thermal and dynamical effects and gives useful insights into non-equilibrium states. However, numerical analysis reveales that for our model we have to extend the London picture by assuming a finite scattering time of the Cooper pairs $\tau_s < \infty$, leading to a damping force acting on the drift velocity which manifests as $1/\omega \to \tau/(1 - i\omega\tau)$. This finite damping is a consequence from the dissipative model as the ω^{-1} pole emerges for a vanishing damping rate $\tilde{\gamma} \to 0$, which corresponds to a junction size of $r_0 \to 0$. There are indications that the relaxation effects in the imaginary response arise from uncertainty between the modes. Let us refer to the set of probing frequencies $\gamma_s < \omega < \omega_{\mathrm{Jp}}$ as the *London probing regime*, in which the response has $\sigma_{2s} \propto \omega^{-1}$ corresponding to the perfect superconductor ($\gamma_s = 0$). Frequencies around $\omega \approx \gamma_s$ form the *relaxation regime*, while frequencies $0 < \omega < \gamma_s$ form the *Hagen-Rubens regime* [Arm09]. The constituents of the fluid are assumed to be independent from each other, so the conductivity is given by the sum of the specific conductivities $\sigma = \sigma_n + \sigma_s = \sigma_1 + i\sigma_2$. In a probing field $\vec{E}(\omega)e^{i\omega t}$, using (2.22), normal electrons $\gamma_n \gg \omega_{\mathrm{Jp}}$ have an ohmic contribution $\sigma_n(\omega) \approx n_n\tau_n$ while Cooper pairs $\gamma_s \ll \omega_{\mathrm{Jp}}$ in the relaxation regime obey

$$\sigma_s(\omega) = \frac{2\pi}{\Phi_0} \frac{e^*d}{\hbar\gamma_s^0} J_{\mathrm{eff}} \left(\frac{\gamma_s^2}{\gamma_s^2 + \omega_p^2} + i\frac{\gamma_s\omega}{\gamma_s^2 + \omega^2} \right), \tag{4.30}$$

where $\gamma_s^0 = \gamma_s(0)$ is the effective coupling γ_s^0 in thermal equilibrium at $T = 0$. The *relaxation energy* $\hbar\gamma_s$ defines the energy scale at which relaxation effects dominate the response. Note that for effective Cooper pair coupling $\gamma_s = 0$, the London picture of a perfect superconductor (4.35) is recovered. In the linear response regime Ohm's law is $I(\omega)d = \sigma(\omega)V(\omega)$. Using the second Josephson relation in phase space representation (4.13), the conductivity in a probing field gets

$$\sigma_s(\omega) = \frac{e_*d}{E_c} \frac{I(\omega)}{\delta n(\omega)}. \tag{4.31}$$

This is the interface to access the system response from a numerical perspective.

4.4.1 Analytical considerations

Adding a viscous damping force described by a typical damping rate γ to (4.4) yields the Resistively and Capacitively Shunted Junction (*RCSJ*) model [McC68]

$$\ddot{\phi} + \gamma\dot{\phi} + \omega_{\mathrm{Jp}}^2 \sin\phi = \omega_{\mathrm{Jp}}^2 \delta I, \qquad (4.32)$$

where $\delta I = I/I_c$. In a homogenous electric field between the sites, the second Josephson relations gets

$$\frac{\partial\phi}{\partial t} = \frac{e_* d}{\hbar} E(t). \qquad (4.33)$$

The linearized equation of motion $\sin\phi \approx \phi$ for $\phi \approx 2n\pi$ can be solved by monochromatic probing ansatz $I(t) = I(\omega)e^{-i\omega t}$, $E(t) = E(\omega)e^{-i\omega t}$. In the linear regime, Ohm's law is local in frequency space $I(\omega) = \sigma(\omega)E(\omega)$, leading to the conductivity

$$\sigma = \frac{2\pi}{\Phi_0} \frac{\hbar e_* d}{E_c} \left(\gamma + i \left(\frac{\omega_{\mathrm{Jp}}^2}{\omega} - \omega \right) \right). \qquad (4.34)$$

Thus, the supercurrent response obtains a $\pi/2$ phase shift in the London picture and for $\omega \ll \omega_{\mathrm{Jp}}$ this contributes to the imaginary part of the conductivity as

$$\sigma_2(\omega) = \frac{2\pi}{\Phi_0} \frac{J_0 e_* d}{\hbar\omega}. \qquad (4.35)$$

In the limit $\omega \ll \omega_{\mathrm{Jp}}^2$, the London picture $\sigma \approx i\sigma_2$ pole is recovered. Another special probing frequency is the plasma frequency $\omega = \omega_{\mathrm{Jp}}$ at which the imaginary response has a real root.

4.4.2 Numerical analysis

For numerical purpose we use the following discretized Fourier transformation

$$f(\omega) = \frac{\Delta t}{T} \sum_{t=t_0}^{t_0+T} f(t)e^{i\omega t}. \qquad (4.36)$$

Since the measurement time T is finite, it is chosen such that the signal is integrated over an integer of cycles $T\omega/(2\pi) \in \mathbb{N}$. For this section we consider a monochromatic probing current $I(\omega) = I_0/2\delta(\omega - \omega_p)$ so that the conductivity gets

$$\sigma(\omega_p) = \frac{I_0}{2} \frac{e_* d}{E_c} \frac{1}{\delta n(\omega)}, \qquad (4.37)$$

with

$$\delta n(\omega) = \frac{\Delta t}{T} \sum_{t=t_0}^{t_0+T} \langle \delta n \mathcal{V}(t_0, t)\rho_S(t_0)\rangle e^{i\omega t}. \qquad (4.38)$$

Before employing numerical calculations, the required size of the Hilbert space was determined in order to be accurate and computationally efficient as well. For a junction having $\eta \sim 0.1$, the conductivity is calculated in the relaxation regime for different $\dim \mathcal{H}$. The minimum dimension at which the response converges is $\dim \mathcal{H} = 13$. If not explicitly stated otherwise, all numerical experiments in this thesis will have $\dim \mathcal{H} = 15$.

We chose $\delta I \sim 10^{-4}$ to be the relative probing amplitude, as this gives a linear response, which was verified by $\sigma(a\delta I) = a\sigma(\delta I)$. Low frequency probing experiments of thermal junctions confirmed the that $\sigma_1 \to n_n \tau_n + n_s \tau_s$ and $\mathrm{Im}\sigma \to \sigma_{2s}$ as $\omega \to 0$. The latter was confirmed by fitting (4.30) to the low frequency response.

Probing around zero crossing

Consider the response around the zero crossing $\sigma_2 = 0$. From (4.34), the junction voltage is given by

$$\frac{e_*}{E_c}\mathrm{Im}V = \mathrm{Im}\delta n(\omega) = -\frac{J_0 \delta I}{2}\frac{1}{\hbar}\frac{\left(\frac{\omega_{\mathrm{Jp}}^2}{\omega} - \omega\right)}{\gamma^2 + \left(\frac{\omega_{\mathrm{Jp}}^2}{\omega} - \omega\right)^2}. \tag{4.39}$$

Fig. 4.5 shows that the analytical expectation matches the numerical calculations (4.39) accurately in the sense that the relative variances of the fit parameters (J_0, δI, ω_{Jp}, γ) are of magnitude $\sim 10^{-5}$. The junction has $E_c = 1s^{-1}$, $J_0 = 9s^{-1}$ and $\tilde{\gamma} = 8.2\omega_{\mathrm{Jp}} \times 10^{-3}$. The plasma frequency ω_{Jp} was determined from the fit and deviates by $\omega_{01}/\omega_{\mathrm{Jp}} = 10^{-5}$ from the transition frequency ω_{01} between the first two energy eigenstates of the system. The linear frequency $\omega_0 \approx 1.05\omega_{\mathrm{Jp}}$ deviates from the plasma frequency as non-linear terms decrease its value, i.e. $\sin\phi = \phi - \phi^3/3! + \mathcal{O}(5)$. As the ratio $\eta \to 0$, the linear frequency eventually matches up with the plasma frequency $\omega_0 \to \omega_{\mathrm{Jp}}$. When thermal fluctuations are present, the response exhibits resonances close to the transition frequencies ω_{ij} between states of opposite parity. This is a footprint of the quantization of the system. Transitions excluded by the parity selection rule are not activated.

Next, the response of the system in the Josephson regime $\eta = 0.11$ to a probing field of frequency $\hbar\omega_0 = \sqrt{J_0 E_c}$ is considered. Numerical calculations show that the effective Josephson energy for a state in thermal equilibrium at $T = 0$ has approximatively the form

$$J_{eff} = J_0 - \Delta J(\omega_0), \tag{4.40}$$

where $\Delta J(\omega_0)$ is a shift of the Josephson energy which only depends on the linear frequency ω_0. The plasma frequency can be expressed in terms of the shift

$$\omega_{\mathrm{Jp}} = \sqrt{E_C(J_0 - \Delta J(\omega_0))}/\hbar. \tag{4.41}$$

By determine the zero-crossing of σ_2, the plasma frequency is determined numerically and thus, the shift ΔJ. Probing at the linear frequency ω_0, according to (4.34), the imaginary
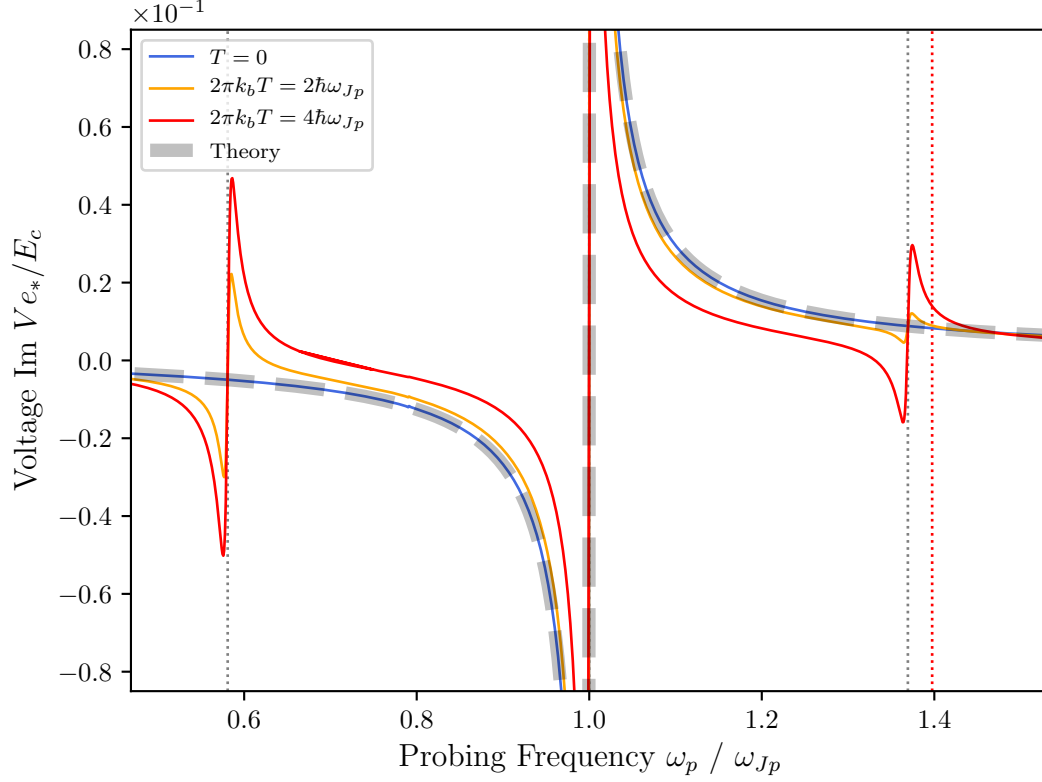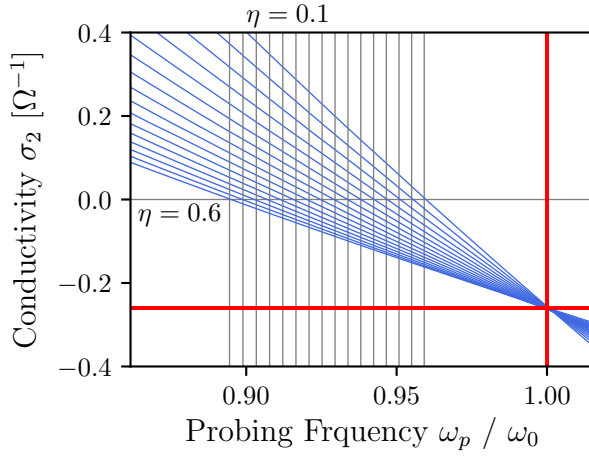
Figure 4.5: **Thermal junction voltage**
Imaginary voltage in a probing field around the plasma frequency for different thermal states. The open dissipation channels $\mathcal{D}A(\pm\omega)$ are depicted as vertical grey lines while the red vertical lines mark transitions which are excluded due to parity. A fit for the analytical prediction (4.39) at $T = 0$ is depicted as grey dashed line.

Figure 4.6: **Crossover frequencies**
Probing response $\sigma_2(\omega_p)$ near plasma resonance for different configurations η in the Josephson regime having a fixed linear frequency ω_0. From (4.40), the plasma frequencies are depicted as vertical lines. The red lines mark the expected intersection at $(\omega_0, \sigma_2(\omega_0))$ according to (4.42).

response is proportional to the shift of the Josephson energy

$$\sigma_2(\omega_0) = -\frac{2\pi}{\Phi_0}e_* d\frac{\Delta J}{\hbar\omega_0}. \tag{4.42}$$

Note that the latter does not depend on the ratio $\eta < 1$ but only on the linear frequency ω_0. The shift ΔJ originates from the cubic term of $\sin\phi$ in the RCSJ model (4.32). For $\eta > 1$, the quintic term becomes relevant as well, which is why this approximation is valid in the Josephson regime. According to (4.37) the shift can also be obtained numerically as

$$\Delta J = -\frac{\Phi_0}{2\pi}\frac{I_0}{2}\frac{1}{\delta n(\omega_0)}J_0. \tag{4.43}$$

Figure 4.6 confirms the expectations drawn from the classical model in the Josephson regime. The conductivity $\sigma_2(\omega_0)$ is independent of $\eta < 1$ for fixed ω_0. The numerically synthesized values of ΔJ match up accurately with the Plasma frequency read from the zero crossing frequency, which supports a correct calibration of the implementation. Linear regression shows that the shift of the Josephson energy is roughly given by $\Delta J/\hbar \approx \frac{\omega_0}{4} + 0.025/s$. In the charge regime, the latter thoughts are not valid as there are no two states bound to the potential (Fig. 4.1).

Thermal zero crossing

At absence of thermal fluctuations, in equilibrium, the groundstate is exclusively occupied. Small probing fields $\delta I \ll 1$ therefore only resonate with the plasma frequency. At $2\pi k_b T/\hbar\omega_{\mathrm{Jp}} > 1$, higher energy states become occupied and thus additional energyscales become available. The probing field may also resonate with these thermally activated transitions. Eventually additional zero-crossings emerge having the same signature as the plasma mode. Figure 4.7 shows that, due to thermal fluctuations, the probing field resonates near
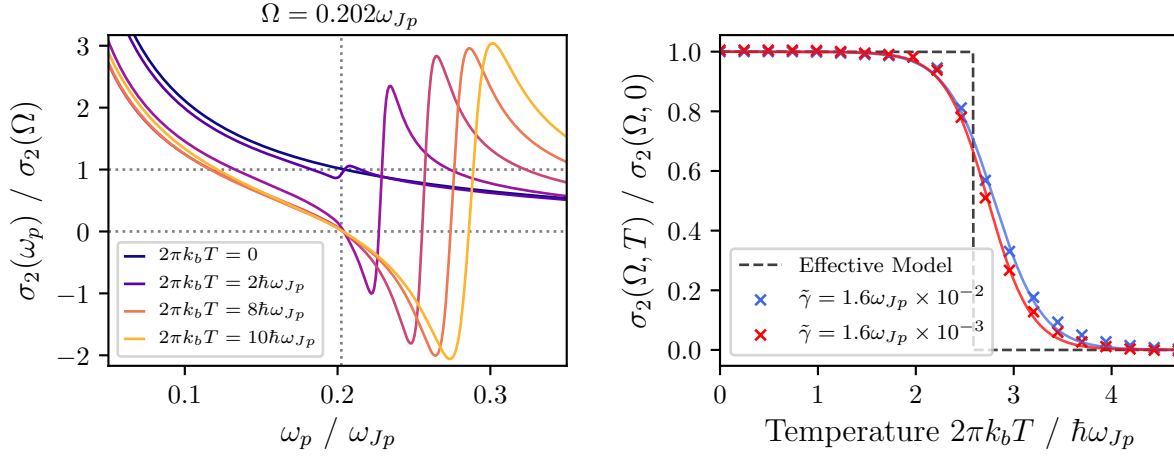
Figure 4.7: **Junction $\eta = 0.5$ in a probing field at different thermal states**
left: Imaginary response within the London probing regime. Thermal fluctuations activate
the transition $\hbar\Omega$ and an additional zero-crossing emerges. **right**: Change of $\sigma_2(\Omega, T)$
relative to the $T = 0$ response at probing frequency close to the transition frequency. A fit
of the Fermi-Dirac distribution is depicted as continuous lines. The dashed lines depict the
$\beta \to \infty$ case where the chemical potential was set to the energy scale synthesized from the
Ω relaxation regime $\mu = \epsilon_\Omega \sim 0.41\omega_{Jp}$.

the transition frequency $\Omega \sim 0.2\omega_{\text{Jp}}$ and a new zero crossing emerges for $2\pi k_b T/\hbar\omega_{\text{Jp}} \gtrsim 4$.
The response shows an additional relaxation regime emerging around $(\omega_p, \sigma_2(\Omega, 0)/2)$ such
that $\sigma_2(\omega_p, T) = \sigma_2(\Omega, 0)/2$. Using (4.30) an effective energy scale $\hbar\epsilon_\Omega$ can be synthesized
from this sub-relaxation regime. The weight $\sigma_2(\Omega, T)/\sigma_2(\Omega, 0)$ fits a Fermi-Dirac distribu-
tion where the chemical potential is approximatively given by the effective energy $\mu = \epsilon_\Omega$.
The dissipative model induces a shift of the crossing frequency $\omega_p \approx \Omega + \gamma_s^{\text{eq}}/2$. Note that
these high temperature features are not due to the dissipative model but are a consequence
from the discrete spectrum of the quantized system.

London probing regime

In the London probing regime, at zero temperature, the response has the form $\sigma_2 \propto \omega^{-1}$
(see Fig. 4.7). As mentioned before, (4.35) motivates a definition of an effective Josephson
energy allowing to gain useful insights into the system at non-equilibrium configurations.
Using (4.31) the response has

$$\left(\text{Im}\frac{1}{\delta n(\omega)}\right)^{-1} = \frac{J_0\delta I}{2}\frac{\omega}{\hbar\omega_{\text{Jp}}^2}. \tag{4.44}$$

However, thermal modes may have a strong influence on the response in the London probing regime as Figure 4.7 shows.

Relaxation regime

In the relaxation regime the imaginary part of the response (4.30) gets

$$\frac{\omega_{\mathrm{Jp}}^2}{\hbar\gamma_s^{\mathrm{eq}}}\frac{\gamma_s\omega}{\gamma_s^2+\omega^2} = \frac{J_0\delta I}{2}\mathrm{Im}\frac{1}{\delta n(\omega)}. \tag{4.45}$$

Around the relaxation energy $\hbar\gamma_s$, the response has a precise Drude form (2.20), where the relative variances of the fit parameters are $\sigma_{J_s}/J_s \sim 2\times 10^{-3}$ and $\sigma_{\gamma_s}/\gamma_s \sim 25\times 10^{-4}$. Figure 4.8 shows the fitting of the imaginary conductivity (4.45). It was possible to extract the plasma frequency of ω_{Jp} from the Drude form as well as the relaxation energy $\gamma_s/\omega_{\mathrm{Jp}} \approx 10^{-3}$, which is a reasonable value considering an imperfect superconductor. For low thermal energies, $\gamma_s(2\pi k_b T < \hbar\omega_{\mathrm{Jp}}) = \gamma_s^0$ is constant, while at $2\pi k_b T \gtrsim \hbar\omega_{\mathrm{Jp}}$ a monotonic increase of the coupling is observed implying that the relaxation energy depends on the thermal fluctuations $\hbar\gamma_s(T)$. This is an expected result as dissipation channels are activated for $2\pi k_b T > \hbar\omega_{\mathrm{Jp}}$. Using the fit parameters from the imaginary conductivity (4.45), the density of normal electrons can be obtained from the differential $n_n \propto (\sigma_1)_i - \sigma_{s1}(\omega_i)$, where $(\sigma_1)_i$ is the full response at probing frequency ω_i. As $2\pi k_b T \gg \hbar\omega_{\mathrm{Jp}}$ the normal conducting electron density obtains a finite value. For small frequencies the differential is approximatively constant indicating $\gamma_n \gg \gamma_s$.

Relaxation effects have their origin in the dissipative model and are not present in the unitary evolution of the reduced system. In the charge regime, the uncertainty between the modes is reduced compared to the Josephson regime. Thus, the relaxation energy decreases $\hbar\gamma_s \to 0$ as the charge energy becomes dominant $\eta \to \infty$. Introducing a non-hermitian operator

$$h = H + \frac{i}{2}\sum_\omega \gamma(\omega)A(\omega)^\dagger A(\omega), \tag{4.46}$$

the generator of the quantum dynamical map takes form

$$\mathcal{L}\rho = -ih\rho + \frac{1}{2}\sum_\omega \gamma(\omega)A(\omega)\rho_S A(\omega)^\dagger + \mathrm{h.c.} \tag{4.47}$$

Recall that terms of form $A\rho A^\dagger$ are referred to as jump terms. In numerical experiments, the jump term was set to zero so that the generator takes the form

$$\mathcal{L}\rho = -ih\rho + \mathrm{h.c.} \tag{4.48}$$

The relaxation regime is still present supporting a connection between a finite relaxation energy $\hbar\gamma_s > 0$ and uncertainty.
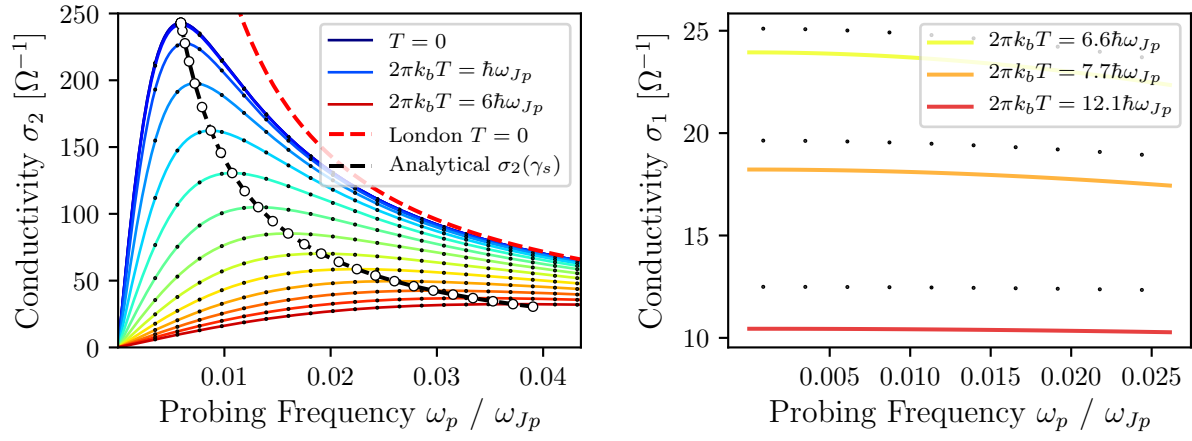
Figure 4.8: **Response to a probing field in the relaxation regime**
left: Fitting of imaginary response $\sigma_2(\omega_p)$ according to (4.49). The perfect London superconductor response at $T = 0$ is depicted as red dashed line. Extrema of σ_2 are at γ_s which are graphed with a black dashed line. **right**: The real conductivity σ_1 (solid lines) is graphed using the parameters J_{eff}, γ_s from the σ_2 fit while the numerical values of σ_1 are depicted as black dots.

4.4.3   Effective Josephson energy

In the last section it was motivated that an effective Josephson energy can be defined within the low probing spectrum. This section will take a closer look at the different regimes and also establishes a numerical synthesizes of the Josephson energy within the relaxation regime. The Josephson energy is proportional to the superfluid density $n_s = \psi^*\psi$ where ψ is the complex order parameter. At temperatures $2\pi k_b T/\hbar\omega_{\mathrm{Jp}} \lesssim 1$ the condensate is transparent to thermal fluctuations, so $J_{\mathrm{eff}}(T) = J_{\mathrm{eff}}(0)$. Thermal energies above the plasma energy lead to excitations of the longitudinal plasma mode decreasing the superfluid density. Thus, the effective Josephson energy is expected to lower monotonically $J_{\mathrm{eff}}(T) < J_{\mathrm{eff}}(0)$ for temperatures above the plasma energy.

First, consider the London probing regime. Due to the relaxation effects, the inverse of the imaginary conductivity is of form $\sigma_2^{-1} \propto \omega_p + a$ where $a = dy/d\omega$ with $y = \sigma_2(\omega)\omega$. Local deviations, due to dynamical control, can be smoothed by regression of a probing sequence. Unfortunately, the slope of σ_2^{-1} depends on the system configuration. For instance, the quantitative outcome of $J_{\mathrm{eff}}(T)$ strongly depends on the damping rate $\tilde{\gamma}$. Thermal modes may also distort the response in the London probing regime (see Fig. 4.7).

Leaving the London probing regime we now move into the relaxation regime. As stated above, using (4.45), the effective Josephson energy J_{eff} can be defined as

$$\frac{J_{\mathrm{eff}}}{\hbar\gamma_s^{\mathrm{eq}}}\frac{\gamma_s\omega_p}{\gamma_s^2 + \omega_p^2} = \frac{\delta I}{2\eta}\mathrm{Im}\frac{1}{\delta n(\omega_p)}. \tag{4.49}$$

Figure 4.9 shows that the latter definition classifies as an order parameter. We note that the relative variances of the fit parameters are $\sigma_J = 2 \times 10^{-3}J_s$ and $\sigma_\gamma = 25 \times 10^{-4}\gamma_s$. For $2\pi k_b T/\hbar\omega_{\mathrm{Jp}} < 1$, the effective Josephson energy is not affected by thermal fluctuations $J_{\mathrm{eff}}(T) = J_{\mathrm{eff}}(0)$. As the thermal energy grows above the plasma energy $2\pi k_b T/\hbar\omega_{\mathrm{Jp}} > 1$, the effective Josephson energy J_{eff} decreases monotonically and thus qualifies as an order parameter. Note that J_{eff} does barely depend on the damping rate $\tilde{\gamma}$. From the effective Josephson energy J_{eff}, we determine the plasma frequency $\hbar\omega_{\mathrm{Jp}} = \sqrt{J_{\mathrm{eff}}E_C}$ which equals the zero-crossing frequency of σ_2 according to (4.34) precisely. In the Josephson regime $\eta < 1$, the plasma frequency equals the transition frequency between the first two bound states.

The relaxation energy $\hbar\gamma_s(T)$ increases according to the Boltzmann factor of the plasma energy

$$\gamma_s(T) = \gamma_s(0)\left[1 + ae^{-\frac{\hbar\omega_{\mathrm{Jp}}}{k_b T}}\right], \tag{4.50}$$

where the explicit expression of a is not pursued any further at this point. As the temperature further builds up $2\pi k_b T/\hbar\omega_{\mathrm{Jp}} \gg 1$, other modes contribute to the relaxation energy. It was checked that the relaxation energy is linear in the damping rate $\gamma_s(a\tilde{\gamma}, T) = a\gamma_s(\tilde{\gamma}, T)$ (See Table 4.1).
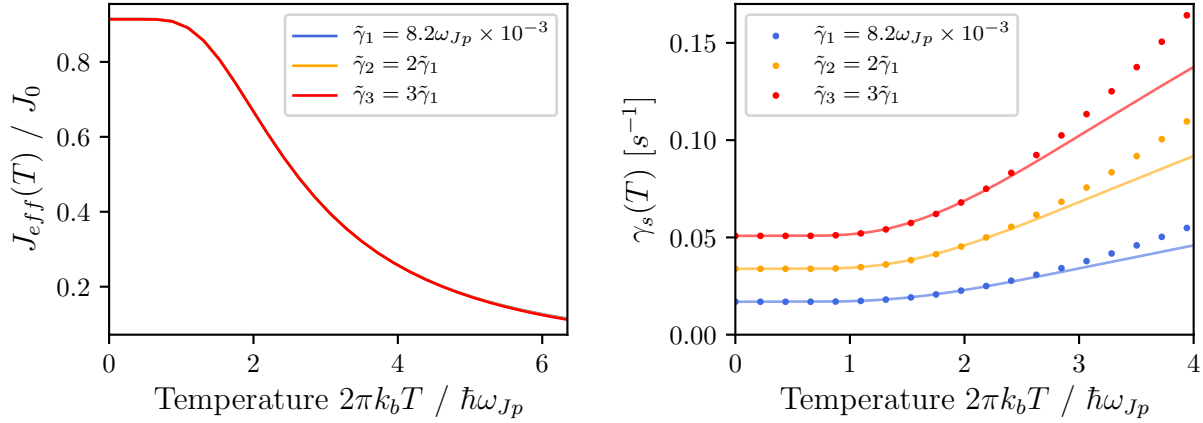
Figure 4.9: **Energy scales in the relaxation regime**
Fitting the parameters $J_{\text{eff}}(T)$, $\gamma_s(T)$ of (4.49) in the relaxation regime. **left**: Effective Josephson energy $J_{\text{eff}}(T)$ at different damping rates $\tilde{\gamma}$. Note that $J_{\text{eff}}(T)$ is not affected by $\tilde{\gamma}$. **right**: Effective damping $\gamma_s(T)$ for different damping rates $\tilde{\gamma}$. The continuous lines are the corresponding Boltzmann rates (4.50) where the value of a was determined from fitting against the numerical values.

Dynamical effects might influence the low frequency part of the probing response. The following definition of a relative error gives an indication of numerical stability by quantifying the deviation from the analytical response (4.49)

$$\delta\sigma_2 = \frac{1}{N}\sqrt{\sum_i \left(\frac{\sigma_2(\omega_i) - \sigma_{2i}}{\sigma_2(\omega_i)}\right)^2} \tag{4.51}$$

For stable configurations, the relative error is usually of magnitude $\sim 10^{-5}$.

E_c [s^{-1}]	J_0 [s^{-1}]	ω_{01} [ω_{Jp}]	ω_{Jp} [s^{-1}]	$\tilde{\gamma}$ [ω_{Jp}]	γ_s^{eq} [$\tilde{\gamma}$]	J_{eff} [J_0]
1.0	9.0	2.8691173	2.869289	0.008233	0.7169	0.915
			2.868936	0.016462	0.7172	0.915
			2.868410	0.024683	0.7175	0.914
1.5	6.0	2.7983573	2.799218	0.007836	0.4656	0.871
			2.799064	0.015670	0.4656	0.871
			2.798838	0.023500	0.4657	0.870
2.0	4.5	2.7259013	2.727699	0.007440	0.3389	0.827
			2.727619	0.014880	0.3389	0.827
			2.727500	0.022318	0.3389	0.827
2.5	3.6	2.6649723	2.668378	0.007120	0.2611	0.791
			2.668325	0.014240	0.2611	0.791
			2.668252	0.021359	0.2611	0.791
3.0	3.0	2.6352753	2.645444	0.006998	0.2053	0.778
			2.645408	0.013996	0.2053	0.778
			2.645362	0.020994	0.2053	0.778

Table 4.1: Characterizing properties of the Josephson junction synthesized from the relaxation regime.

4.5 Current fluctuations

The fluctuations of the current are given by

$$V = \left\langle \sin^2 \theta \right\rangle - \left\langle \sin \theta \right\rangle^2. \tag{4.52}$$

Due to symmetry, the expectation value of the junction current vanishes at thermal equilibrium

$$\left\langle \sin \theta \right\rangle = 0. \tag{4.53}$$

Using (4.27) the current fluctuations converge to $V = 0.5$ as $T \to \infty$ as the state is $\sim \mathrm{Id}_S$.

The current flucutations are obtained by taking the mean value of $V(t)$ after the transient evolution gets into a steady state. From the Fourier transform, the mean value is given as

$$V_0 = \mathcal{F}[\sin^2 \phi](\omega = 0). \tag{4.54}$$

For different dynamical setups, the time in which transient phenomena occur vary strongly. This motivates a definition of a measure to quantify whether the system is in steady state. Taking the mean $j(\mathcal{I}_i)$ over N different intervals $\mathcal{I}_i$, allows comparing $j(\mathcal{I}_i)$ to the full signal V_0

$$\sigma^2_{V_0} = \sum_i \left(V_0(\mathcal{I}_i) \right) - V_0 \Big)^2. \tag{4.55}$$

Therefore, $\sigma^2_{V_0} > 0$ indicates that V_0 contains transient contributions.

4.6 Harmonic limit

In the last sections, the origin of the relaxation regime, which is a consequence of the dissipative model, was discussed. We've revealed indications, that the relaxation energy relates to uncertainty of modes. In this section, the Hamiltonian (4.11) is approximated as a harmonic oscillator, by defining canonical annihilation and creation operators from the conjugate variables. A numerical implementation allows to compare the energy scales between the original and the linear system.

Using the conjugate observables ϕ and δn, one can construct canonical annihilation and creation operators

$$a = \sqrt{\frac{\hbar \omega_0}{2 E_C}} \phi + i \sqrt{\frac{E_C}{2 \hbar \omega_0}} \delta n. \tag{4.56}$$

This allows to map onto the driven harmonic oscillator

$$H = \hbar \omega_0 a^\dagger a + E_C^{-1} I_e(t) \phi, \tag{4.57}$$

with the linearized phase operator

$$\phi = \sqrt{\frac{E_C}{2\omega_0}} \left(a^\dagger + a\right).$$

From (4.56) the charge operator is determined to be

$$\delta n = -i\sqrt{\frac{\hbar\omega_0}{2E_C}} \left(a - a^\dagger\right). \tag{4.58}$$

Thus, the potential energy from the dipole operator (4.16) in the electric field gets

$$H_I = i\sqrt{\frac{e_*^2 r_0^2 \hbar\omega_0}{2E_C}} \left(a - a^\dagger\right) \otimes E. \tag{4.59}$$

In the optical limit, the generator of the non-unitary dynamics obtains Lindblad form (3.32) and the damping rate (3.45) gets $\gamma(\omega) = \kappa\omega^3(1 + N(\omega))$. The constant

$$\kappa = \frac{\hbar\omega_0}{2E_C} \frac{4e_*^2 r_0^2}{3\hbar\epsilon_0 c^3}, \tag{4.60}$$

is analogous to (4.22). The master equation gets

$$\mathcal{L}\rho = -\frac{i}{\hbar}\left[H_S, \rho\right] + \kappa\omega_0^3(1 + N(\omega_0))\mathcal{D}a\rho + \kappa\omega_0^3\mathcal{D}a^\dagger\rho. \tag{4.61}$$

Note that, in contrast to the nonlinear system, the transition operator has $(\dim H - 1)$ non zero elements. We define the driving Hamiltonian

$$H_{\mathrm{drv}} = \hbar\omega_f(t) \left(a + a^\dagger\right)^2. \tag{4.62}$$

Appendix C provides the matrix representations of the operators which are used in the numerical analysis.

The linear frequency ω_0 characterizes the energy scale of the system and equals the plasma frequency. Using (4.34), the zero-crossing occurs at the linear frequency, which is numerically confirmed. In the harmonic limit, modes are coupled leading to a finite relaxation energy. This is confirmed as for $\omega_p \to 0$ the relaxation regime becomes eminent. From the relaxation regime (4.49), the plasma energy is determined to be $\hbar\omega_0$.

Chapter 5

Dynamical control

Non-equilibrium physics have gathered a lot of attention over the last decade. Analytical methods are a powerful tool to analyze non-equilibrium physics in certain limits. On the other hand, numerical methods provide access to non-equilibrium states beyond analytical landscapes. When numerical analysis is in harmony with analytical considerations, one can explore more sophisticated limits numerically, just by tuning the simulation parameters. In the last chapter we have established a numerical framework capable of synthesizing properties like the current fluctuations and the linear response in an AC probing field. In this chapter, we will use this numerical framework to analyze the properties of a dynamically controlled Josephson junction.

5.1   Parametric driving

Recent studies by Okamoto et al. point out that parametric driving provides a mechanism capable of enhancing the optical superconducting properties in a bilayer system [OCM16a, OHCM17]. Modulation of the Josephson energy affects the low frequency response of the junction in a probing field. For this chapter, we will consider a parametric driving Hamiltonian of form

$$H_d(t) = J_0 A \cos\left(\omega_d t\right) \cos \phi, \tag{5.1}$$

where A is the *driving amplitude* and ω_d the *driving frequency*. The equation of motion is obtained by extending the RCSJ model (4.32) as

$$\ddot{\phi} + \gamma\dot{\phi} + \omega_0^2(1 + A\cos(\omega_d t))\sin\phi = I_0\cos(\omega_p t). \tag{5.2}$$

In the limit of small phase $\sin\phi \approx \phi$, going into frequency space by Fourier transforming the equation of motion, one obtains a set of linear equations corresponding to the harmonics of $\cos\left(\omega_d t\right)$, which is solved by matrix inversion[OCM16a]. Truncating higher harmonic contributions $(m = 1)$ and solving a set of three linear equations gives the conductivity

$$\sigma(\omega_p) = \frac{2\pi}{\Phi_0} \frac{\hbar e_* d}{iE_c\omega_p} \left[\frac{A^2\omega_{\mathrm{Jp}}}{4} \left(C_+(\omega_p) + C_-(\omega_p)\right) + \omega_p^2 + i\gamma\omega_p - \omega_{\mathrm{Jp}}^2 \right], \tag{5.3}$$

where $C_\pm(\omega_p) = (\omega_{\mathrm{Jp}}^2 - (\omega_d \pm \omega_p)(\mp i\gamma + \omega_d \pm \omega_p))^{-1}$. Therefore, a pole in the low frequency domain is identified at

$$\omega_* = \omega_{\mathrm{Jp}} - \omega_d.$$

Numerical pump-probe experiments in this section are set up as follows: The simulation time is chosen such that the lowest probe oscillation performs 4 full cycles, i.e. $T\omega_{p,0} = 8\pi$. The lowest probing frequency is chosen such that $\omega_{\mathrm{Jp}}/\omega_{p,0} \sim 10^3$ cycles of the plasma oscillation are included in each run Higher frequencies $\omega_p > \omega_{p,0}$ are probed over a period T', such that $0 \leq (T - T')\omega_p < 2\pi$.

The upcoming sections are structured as follows: First, the parametric enhancement within the Josephson regime is captured. In the second section, thermal modes are coupled to the probe pulse. The last three sections capture the dynamical properties of the parametrically driven junction, by synthesizing the energy scales characterizing the relaxation regime.
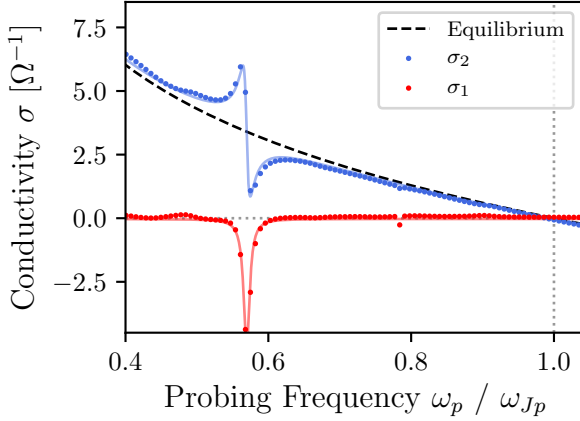
Figure 5.1: **Josephson Regime**
Parametrically driven junction $\eta = 0.11$ at $T = 0$ having $\tilde{\gamma} \sim 8.2\omega_{\text{Jp}} \times 10^{-3}$ compared to the analytical model (5.3). All parameters but γ are set to the actual values from the simulation. The corresponding classical damping rate $\gamma = 0.0287s^{-1}$ was determined by fitting the model. The analytical model is depicted as continuous graphs, while the numerical data is depicted as dots.

5.2 Parametric enhancement

In this section, the pump-probe experiments are performed in the Josephson regime $\eta = 0.11$. As parametric driving is applied, the response crosses the equilibrium conductivity at $|\omega_*|$. At probing frequencies below the pole $\omega_p < \omega_*$, the imaginary conductivity is enhanced by $\sim 10\%$ compared to the equilibrium response, which qualitatively agrees with studies by Okamoto et al. [OCM16a, Hom18]. The real conductivity σ_1 is negative for frequencies near ω_*, thus the applied electrical field gets amplified by the current response. Figure 5.1 compares the classical model (5.3) to the numerical response. From fitting the model (5.3), a classical damping rate of $\gamma = 0.0287s^{-1}$ was determined, where the actual parameters from the simulation (E_C, ω_{Jp}, A, ω_d) were fixed. Using the latter parameters, the analytical model matches the numerical response accurately.

Parametric driving affects the energy scales J_{eff} and $\hbar\gamma_s$ leading to a renormalization of the relaxation regime. Red-detuned pump pulses $\omega_d < \omega_{\text{Jp}}$ decrease (increase) the effective Josephson energy (relaxation energy), while blue-detuned driving $\omega_{\text{Jp}} < \omega_d < \frac{3}{2}\omega_{\text{Jp}}$ increases (decreases) the effective Josephson energy (relaxation energy).

Figure 5.2 shows that above a driving frequency of $\omega_d \gtrsim 1.6\omega_{\text{Jp}}$ the response is not consistent with the linear model. The real part of the conductivity shows band structures in this regime, where we leave the origin of those features open at this point. The rich variety of features might be due to the fact that, in the Josephson regime, several transition frequencies $0.6\omega_{\text{Jp}} < \omega_{ij} < \omega_{\text{Jp}}$ exist (See Fig. 4.1), to which the pump pulse couples. Thermal fluctuations convolve the signal as they increase the relaxation energy. Pumping a high temperature junction at a frequency of $\omega_d \sim 1.5\omega_{\text{Jp}}$, a strong enhancement of the imaginary conductivity σ_2 is observed and the real conductivity σ_1 drops below zero.
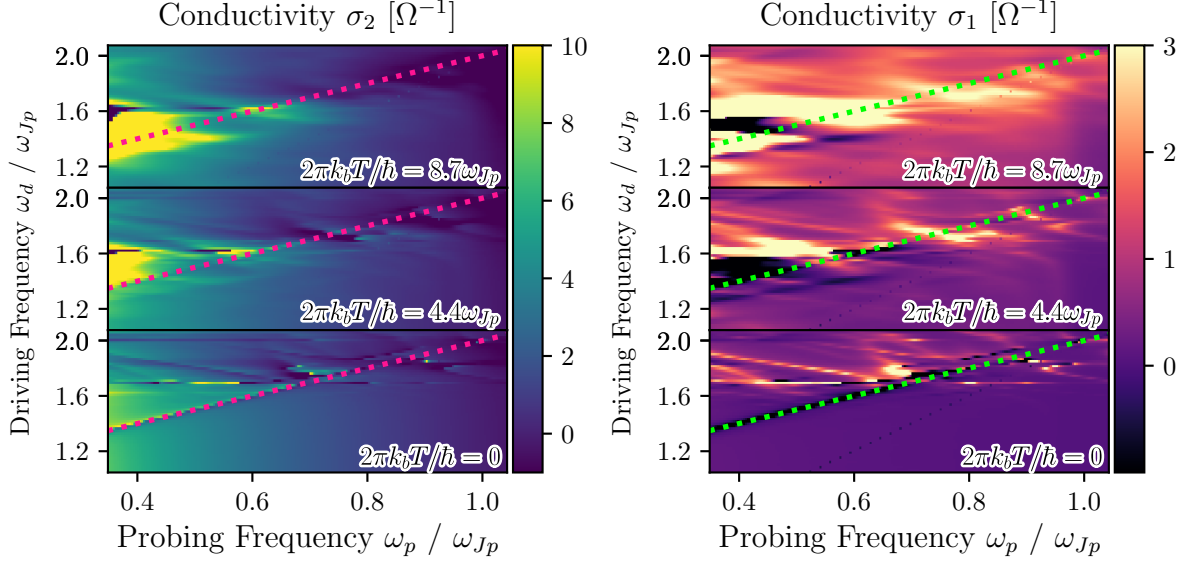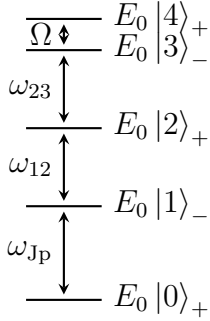
Figure 5.2: **Steady state parametric driving - frequency field**
Junction at $\eta = 0.11$ having a damping rate of $\tilde{\gamma} \sim 8.2\omega_{\mathrm{Jp}} \times 10^{-3}$ for three different thermal states. The driving amplitude is fixed to $A = 0.1$. The dotted lines indicate the poles ω_* according to (5.3).

5.3   Parametric coupling to thermal modes

Consider a junction close to the charge regime $\eta \sim 0.5$. We choose the ratio η such that two distinct transition frequencies are located in the low frequency part $\omega_p < \omega_{\mathrm{Jp}}$ of the probing spectrum (see Fig. 4.1). The first frequency $\Omega \sim 0.26\omega_{\mathrm{Jp}}$ is the transition frequency between the last two non-degenerate states from the spectrum. The second frequency $\omega_{12} \sim 0.84\omega_{\mathrm{Jp}}$ corresponds to the transition between the first and the second excited state. In this setup, the transition frequency ω_{12} equals the transition frequency between the second and the third exited state of the spectrum ω_{23}, which is why we will only include ω_{12} into the upcoming discussions.

Figure 5.3 shows three different numerical steady state pump-probe experiments of a Josephson junction near the charge regime. At absence of thermal fluctuations, the ω_* pole is observed. The superconductive response for probing frequencies below the pole $\omega_p < \omega_*$ is enhanced by $\sim 10\%$ compared to the undriven case. Next, the same pump-probe experiment was performed for a junction at high thermal energy $2\pi k_b T/\hbar\omega_{\mathrm{Jp}} \gg 1$. A strong enhancement of the superconductive response of $\sim 100\%$ takes place. Furthermore, the
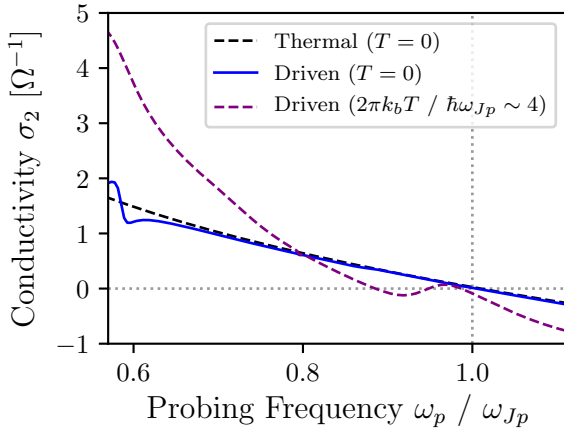
Figure 5.3: **High T charge regime** Parametrically driven junction $\eta = 0.44$ having a damping rate of $\tilde{\gamma} \sim 2.2\omega_{\text{Jp}} \times 10^{-2}$. The thermal equilibrium response at $T = 0$ is depicted as black dashed line, while the parametrically driven junction response at $T = 0$ is depicted as blue line. A parametrically driven high temperature junction is depicted as purple dashed line. The pump pulse has the driving frequency $\omega_d \sim 1.59\omega_{\text{Jp}}$ and the driving amplitude $A = 0.1$.

response obeys additional changes of curvature in the probing spectrum close to the plasma frequency $\omega_p \sim 0.9\omega_{\text{Jp}}$. Comparing this result to [OCM16a](Fig. 1), [Hom18](Fig 5.7), qualitative agreements stand out: The conductivity is enhanced by a factor of ~ 2 and similar features in the qualitative form of σ_2 are present near $\omega_p \sim \omega_{\text{Jp}}$. Note that the experimental data belong to a transient state, while a steady state was probed in this section.

Let us focus on the role of thermal fluctuations. Fig. 5.4 shows a parametrically driven junction ($\omega_* \sim 0.44\omega_{\text{Jp}}$) at different thermal states, as well as the equilibrium junction at different damping rates $\tilde{\gamma}$. At the absence of thermal fluctuation, parametric driving induces two poles $\omega_* \sim 0.44\omega_{\text{Jp}}$, $\omega_x \sim 0.13\omega_{\text{Jp}}$. The response at probing frequencies below $\omega_p < \omega_*, \omega_x$ is enhanced. Thermal Ω, ω_{12} modes are not activated by the pump pulse. At presence of thermal fluctuations $2\pi k_b T/\hbar\omega_{\text{Jp}} = 3.42$, the thermal modes are activated. Thermal fluctuations renormalize the parametric pole $\omega_*(T) = \omega_d - \omega_{\text{Jp}}(T)$. The pump pulse couples to the thermal modes, i.e. activates the Ω mode. Additionally, a pole at $\omega_p \sim 0.54\omega_{\text{Jp}}$ emerges and the response is enhanced for $\omega_p > 0.54\omega_{\text{Jp}}$. Going to even higher temperatures $2\pi k_b T/\hbar\omega_{\text{Jp}} = 4.56$ the response above $\omega_p > 0.54\omega_{\text{Jp}}$ is even more enhanced. Note that the enhancement of σ_2 near $\omega_p \sim 0.54\omega_{\text{Jp}}$ does not appear in the equilibrium response.

Different pump frequencies are compared in Figure 5.5. At driving frequencies $\omega_d < 1.4\omega_{\text{Jp}}$ and $\omega_d > 2\omega_{\text{Jp}}$ the global response is barely different from the thermal equilibrium response. The Ω, ω_{12} modes are not fully activated in equilibrium as well as under parametric driving. As the driving frequency increases, the Ω mode is influenced by the pump pulse. Driving the junction at a pump frequency of $\omega_d = 1.65\omega_{\text{Jp}}$ builds up the thermal Ω mode significantly. This may indicate an effective heating of the system due to the pump pulse. At higher thermal states, this effect is even stronger leading to an enhancement of the
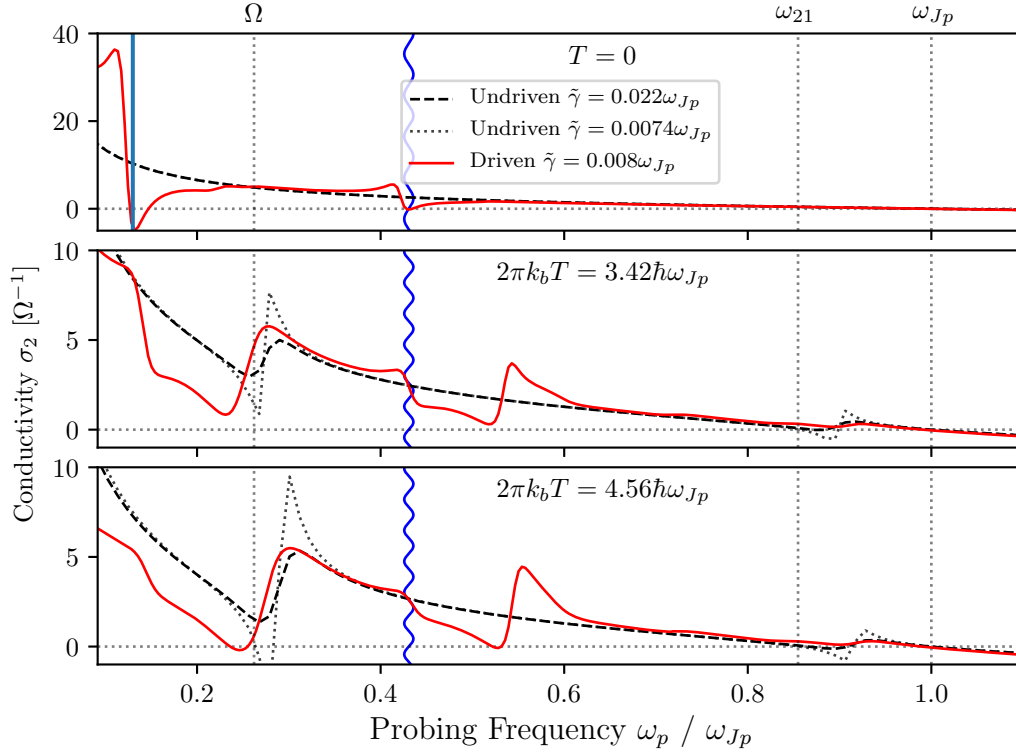
Figure 5.4: **Parametrically induced thermal mode enhancement**
Parametrically blue driven junction $\eta = 0.44$ with a damping rate of $\tilde{\gamma} = 2.2 \times 10^{-2}\omega_{\mathrm{Jp}}$.
The driving pulse (indicated at ω_* as blue vertical wave) has strong influence on the equilibrium response. As thermal fluctuations grow, an additional enhancement appears at $\omega_p \sim 0.55\omega_{\mathrm{Jp}}$. The vertical dotted lines mark the frequencies Ω, ω_{12} and the plasma frequency ω_{Jp}.

imaginary conductivity of $\sim 300\%$. Strikingly, the Ω mode zero-crossing stays close to $\omega_p = \Omega$, which is why we identify the enhancement by the Ω mode itself. Note that the zero-crossing $\omega_p \sim \omega_{\mathrm{Jp}}$, due to the plasma mode, is present at all driving frequencies ω_d.

The ω_{12} mode induces a change of curvature in the response for probing frequencies near the plasma frequency. At $\omega_d = 1.93\omega_{\mathrm{Jp}}$ and $2\pi k_b T/\hbar\omega_{\mathrm{Jp}} = 4.75$ the ω_{12} mode is amplified by the driving. This amplification is not present at higher temperatures as the effective bath coupling is increased.

A high resolution temperature dependence is given in Figure 5.6 for the real and imaginary current response. An additional pole $\omega^\dagger = 2\omega_{\mathrm{Jp}} - \omega_d$ is observed where we leave the origin open at this point. The real conductivity shows several regimes of negative feedback. While parametric driving $\omega_* \gtrsim \Omega$ strongly controls the Ω mode, the ω_{12} mode is barely
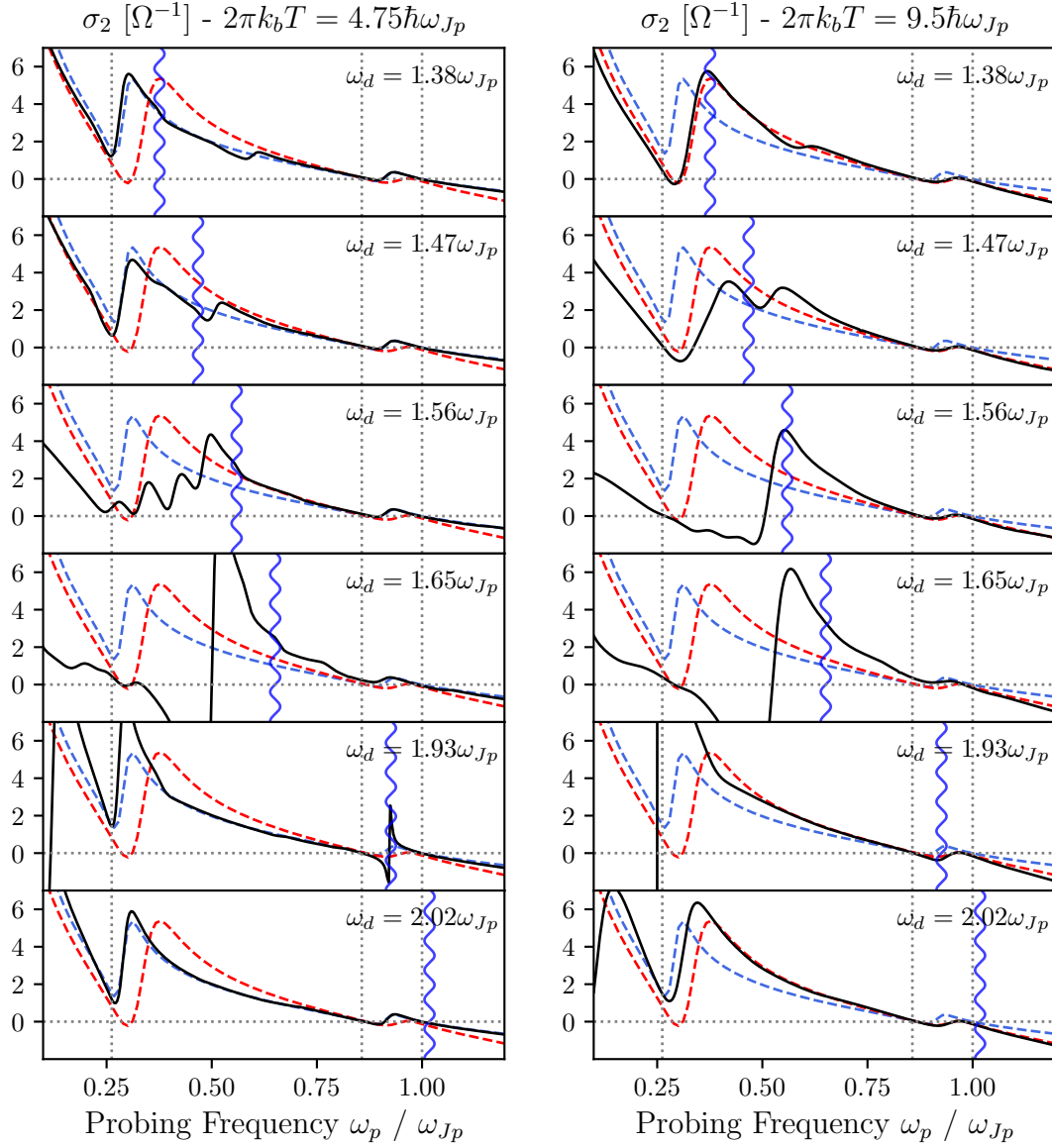
Figure 5.5: **Dynamical control of thermal modes (1)**
Parametrically blue driven junction $\eta = 0.44$ at $\tilde{\gamma} = 2.2\omega_{\mathrm{Jp}} \times 10^{-2}$. Thermal poles (see Fig. 4.7) are influenced by the pump pulse. The blue (red) dashed line is the equilibrium response at $2\pi k_b T = 4.75\omega_{\mathrm{Jp}}$ ($2\pi k_b T = 9.5\omega_{\mathrm{Jp}}$). The vertical dotted lines mark transitions between the states. The blue vertical wiggled line indicates the pole ω_*. The driven σ_2 response is graphed as a black line. All pump pulses have a fixed driving amplitude of $A = 0.1$.
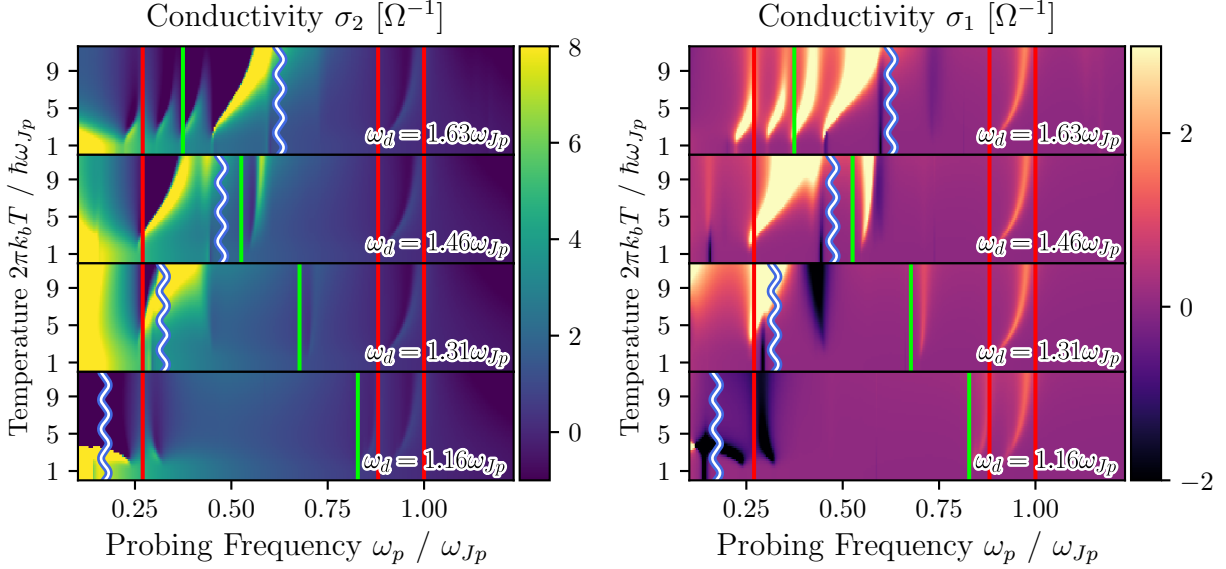
Figure 5.6: **Dynamical control of thermal modes (2)**
Junction at $\eta = 0.44$ having damping $\tilde{\gamma} \sim 7.4\omega_{\mathrm{Jp}} \times 10^{-3}$ at four different driving frequencies ω_d having fixed driving amplitudes $A = 0.1$. The vertical blue waves indicate the poles ω_*, according to (5.3). The modes Ω, ω_{12} and ω_{Jp} are depicted as vertical red lines. Green vertical lines mark the $\omega^\dagger$ poles.

unaffected. It is clearly visible that a driving frequency of $\omega_d \gtrsim 1.63\omega_{\mathrm{Jp}}$ renormalizes the Ω mode.

In this section we have set up a junction such that two transition frequencies Ω, ω_{12} below the plasma frequency ω_{Jp} are present. Thermal fluctuations activate thermal modes corresponding to the latter frequencies. The pump pulse is able to couple to the thermal modes.

5.4 J_{eff} Fano-Feshbach resonance

In the last section the effects of parametric driving, on the low frequency response of the system, was discussed. Now we turn onto driving at red-detuned ($\omega_d < \omega_{\mathrm{Jp}}$) and blue-detuned ($\omega_d > \omega_{\mathrm{Jp}}$) pump frequencies. In this section, using (4.49), the effective Josephson energy in the relaxation regime is compared to the analytical considerations within the London picture.

From the conductivity (5.3), the effective Josephs energy in the London picture evaluates

to

$$J_{\text{eff}} = \lim_{\omega \to 0} \text{Im}\sigma_2 \omega = J_0 \left[1 - \frac{A^2 \omega_{\text{Jp}}^2 (\omega_{\text{Jp}}^2 - \omega_d^2)}{2(\omega_{\text{Jp}}^2 - \omega_d^2)^2 + 2\gamma^2 \omega_d^2} \right]. \tag{5.4}$$

This is a Fano-Feshbach resonance around ω_{Jp}. Numerical pump-probe experiments show that the relaxation regime is stable ($\delta\sigma_2 < 10^{-3}$) for many driving configurations at $\dim\mathcal{H} = 15$. A sequence of probing frequencies in the relaxation regime $\omega_p \sim \gamma_s$ is employed and by fitting (4.49), the effective Josephson energy of the driven system is read out.

5.4.1 Thermal resonance in the Josephson regime

In the Josephson regime, the Fano-Feshbach form (5.4) was confirmed at the absence of thermal fluctuations $T = 0$. Due to higher orders in $\sin\phi$, the anti-symmetric form of $J_{\text{eff}}(\omega_d)$ around ω_{Jp} is distorted as shown in Figure 5.7. In contrast, in the charge regime $\eta > 1$, the Fano-Feshbach resonance disappears. Therefore, the linear model (5.3) is valid in the Josephson regime. It was possible to determine the actual model parameters from fitting the numerical $J_{\text{eff}}(\omega_d)$ with an accuracy of 0.9. Therefore, the extended definition of the effective Josephson energy (4.49) is in harmony with the London picture analytical model (5.4). The effective Josephson energy is transparent to thermal fluctuations $2\pi k_b T / \hbar\omega_{\text{Jp}} \lesssim 1$. Higher temperatures lead to a global decrease of J_{eff} (compare Fig. 4.9). Additional features emerge at temperatures of $2\pi k_b T / \hbar\omega_{\text{Jp}} \gtrsim 2$, which we could not identify with known energy scales of the system so far. Nevertheless, fitting the high temperature effective Josephson energy $J_{\text{eff}}(T, \omega_d)$ still yields fairly accurate model parameters.[1] The classical damping rate increases as thermal fluctuations increase. This is an effect from the dissipative model.[2]

5.4.2 Transition from the Josephson to the charge regime

Consider a fixed linear frequency ω_0. The Fano-Feshbach form (5.4) is confirmed for $\eta \ll 1$. As the charge energy becomes the dominating energy scale, the functional form of $J_{\text{eff}}(\omega_d)$ deviates from the Fano-Feshbach form (5.4) as Figure 5.7 shows. For $\eta \ll 1$ the effective plasma frequency equals the root of the effective Josephson energy $J_{\text{eff}}(\omega_{\text{Jp}}) = 0$. On the other hand, in the charge regime $\eta \gtrsim 1$, a peak $\max_{\omega_d} J_{\text{eff}}(\omega_d) = J_{\text{eff}}(\omega_{\text{Jp}})$ arises. A crucial difference between the two regimes is that in the Josephson regime the plasma mode corresponds to the transition between the first two bound states of the spectrum, which is not the case in the charge regime.

---

[1] The deviation of the fit parameters, compared to the parameters from the simulation, is below 0.2.

[2] The rate at which transitions between states occur is $\gamma(\omega) \sim \omega^3(1 + N(\omega))$, where $N(\omega)$ is the mean number occupation of the bath mode ω.
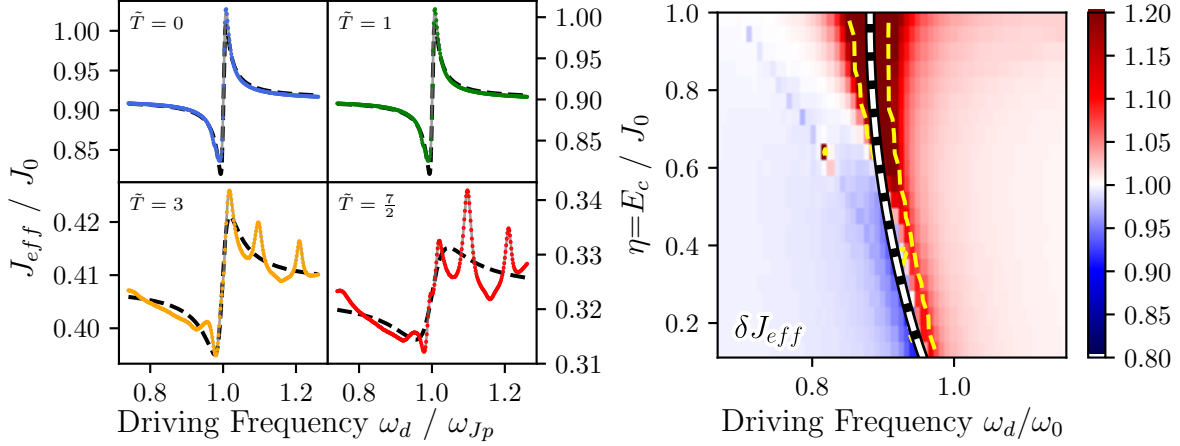
Figure 5.7: **Fano-Feshbach resonance**
left: Thermal effective Josephson energy near $\omega_d \sim \omega_{\mathrm{Jp}}$ in the Josephson regime $\eta = 0.11$. The analytical form (5.4) is depicted as dashed lines and was fitted against the numerical effective Josephson energy $J_{\mathrm{eff}}(\omega_d)$ (dots). **right**: Transition from the Josephson to the charge regime. Relative change of the effective Josephson energy δJ_{eff} due to parametric driving near resonance. The yellow contour borders regions having a relative fit error of $\delta\sigma_2 > 10^{-3}$. The numerical plasma frequency is depicted as white dashed line.

5.4.3   Resonance in the harmonic limit

In the harmonic limit (4.57), the junction was driven using (4.62). The effective Josephson energy J_{eff} was calculated analogous to the full system, using (4.49). Figure 5.4.3 shows the Fano-Feshbach resonance in the harmonic limit. The effective Josephson energy in equilibrium equals the bare Josephson energy $J_{\mathrm{eff}} = J_0$. Thus, the linear frequency equals the plasma frequency $\omega_{\mathrm{Jp}} = \omega_0$. This is confirmed by the Fano-Feshbach resonance (5.4) around $\omega_d = \omega_{\mathrm{Jp}}$. Fitting the analytical model yields the correct values of the parameters $(A, \omega_{\mathrm{Jp}}, J_0)$. The classical damping rate was determined to be $\gamma \sim 1.175\tilde{\gamma}$.

5.5   Parametric driving field

The surface of the Josephson energy $J_{\mathrm{eff}}(A, \omega_d)$ shows very complex features due to parametric driving. The pump-probe experiment in the last sections modulated the Josephson energy at driving frequencies near the plasma frequency $\omega_d \sim \omega_{\mathrm{Jp}}$. In this section, the relative change of the Josephson energy and the relaxation energy is of interest

$$\delta J_{\mathrm{eff}} = \frac{J_{\mathrm{eff}}}{J_{\mathrm{eff}}^0} \qquad \delta\gamma_s = \frac{\gamma_s}{\gamma_s^0}. \tag{5.5}$$
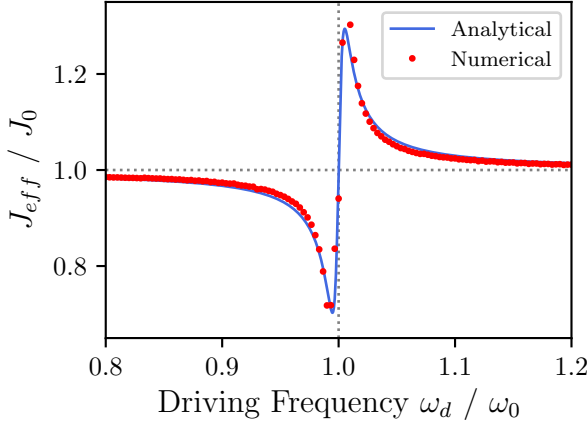
Figure 5.8: **Harmonic limit**
Parametrically driven (4.62) harmonic oscillator (4.57). The effective Josephson energy is synthesized using (4.49) and is compared to the analytical model (5.4). The damping rate is $\tilde{\gamma} = 9\omega_0 \times 10^{-3}$.

First, parametric driving far from the plasma frequency is discussed. Several regimes appear unstable in the sense that the relaxation regime deviates from the Drude form (4.49). Landau and Lifschitz provide analytical insights into the stability of the parametrically driving pendulum [LL97]. The junctions in this section are set up in the Josephson regime ($\eta = 0.11$) and in the charge regime ($\eta = 1$). At the end of the section, a strong enhancement of the effective Josephson energy is presented.

Figure 5.9 shows the parametric driving field within the Josephson regime. For blue-detuned driving frequencies $\omega_d \gtrsim \omega_{\mathrm{Jp}}$, the effective Josephson energy J_{eff} is enhanced for $A \lesssim 0.4$. The relaxation energy $\hbar\gamma_s$ is reduced in this regime corresponding to a decoupling of modes. At greater driving amplitudes, the relaxation regime becomes unstable. Near $\omega_d = 3\omega_{\mathrm{Jp}}$ an additional Reso-Feshbach resonance emerges. Around $\omega_d = 2\omega_{\mathrm{Jp}}$, parametric driving leads to a strong enhancement of current fluctuations V_0. This has a strong influence on the low frequency part of the dynamics as the relaxation regime becomes unstable $\sigma_2 > 5 \times 10^{-3}$. At high amplitude driving $A \gtrsim 0.4$, the truncation of the Hilbert space may induce boundary effects, which destabilize the relaxation regime as well. In Section 4.4.2, we discussed that boundary effects must not be present to stabilize the relaxation regime. Appendix D provides a high resolution parametric driving field near the plasma resonance.

Figure 5.10 shows the parametric driving field within the charge regime. The global qualitative picture is very different compared to the Josephson regime (see Fig. 5.9). Also, the fluctuations of current do not correspond to numerical unstable regime as it was the case in the Josephson regime. An enhancement of the effective Josephson energy was observed for blue-detuned as well as red-detuned pump pulses. While in the Josephson regime the effective Josephson energy J_{eff} and the relaxation energy $\hbar\gamma_s$ behave contrary, in the charge regime this is only partially the case.
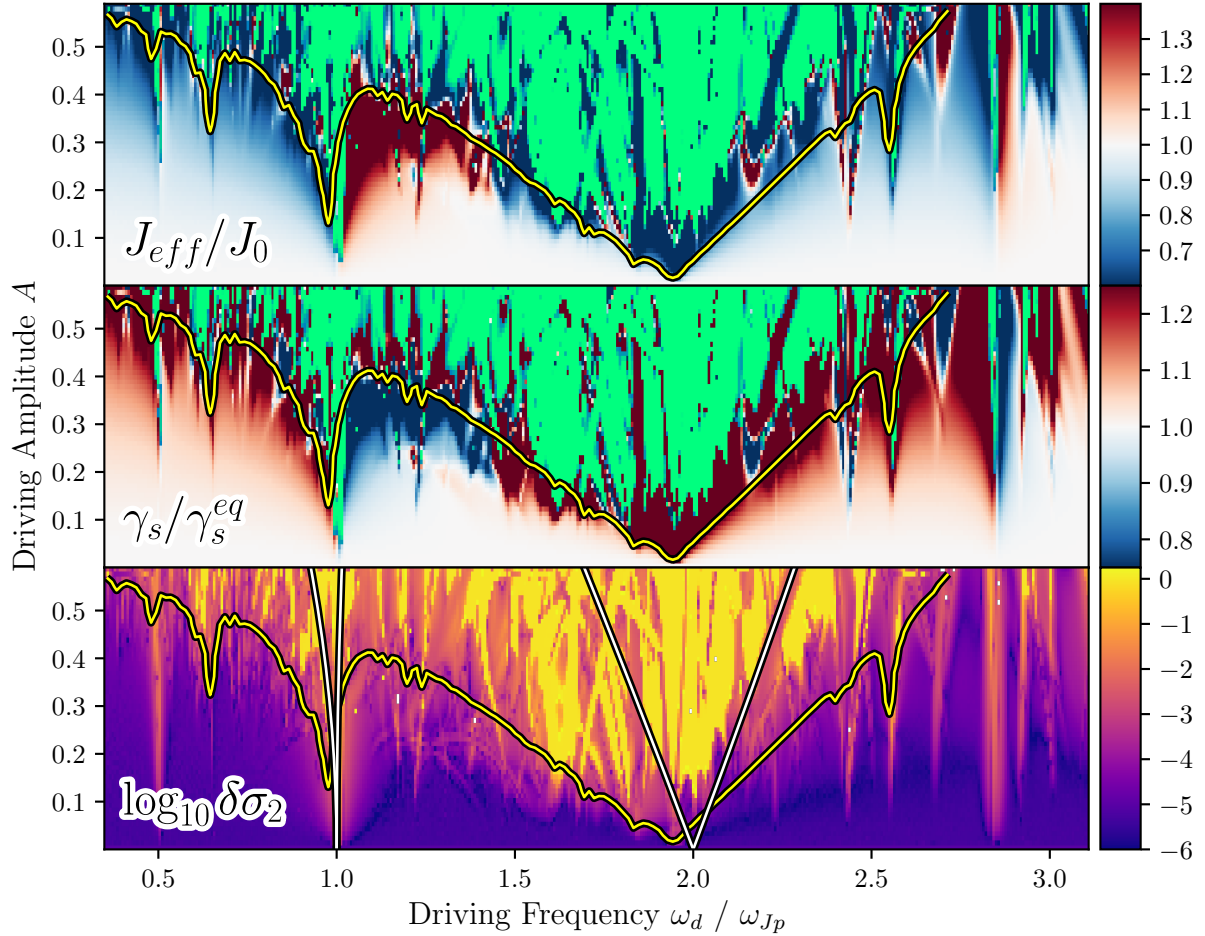
Figure 5.9: **Josephson regime parametric driving field**
Parametric driving $f(t) = A\sin(\omega_d t)$ contour plots for $\eta = 0.11$ at $T = 0$ and $\tilde{\gamma} = 8.3\omega_{\mathrm{Jp}} \times 10^{-3}$. Driving amplitudes above the yellow contour enhance the current fluctuations V_0 by more than 7.5%. **Top two rows**: Relative change of the effective Josephson energy J_{eff} and the effective relaxation energy $\hbar\gamma_s$ compared to equilibrium. Numerical unstable regions ($\delta\sigma_2 > 5 \times 10^{-3}$) are depicted green. **Bottom row**: relative error on logarithmic scale $\log_{10}\delta\sigma_2$.
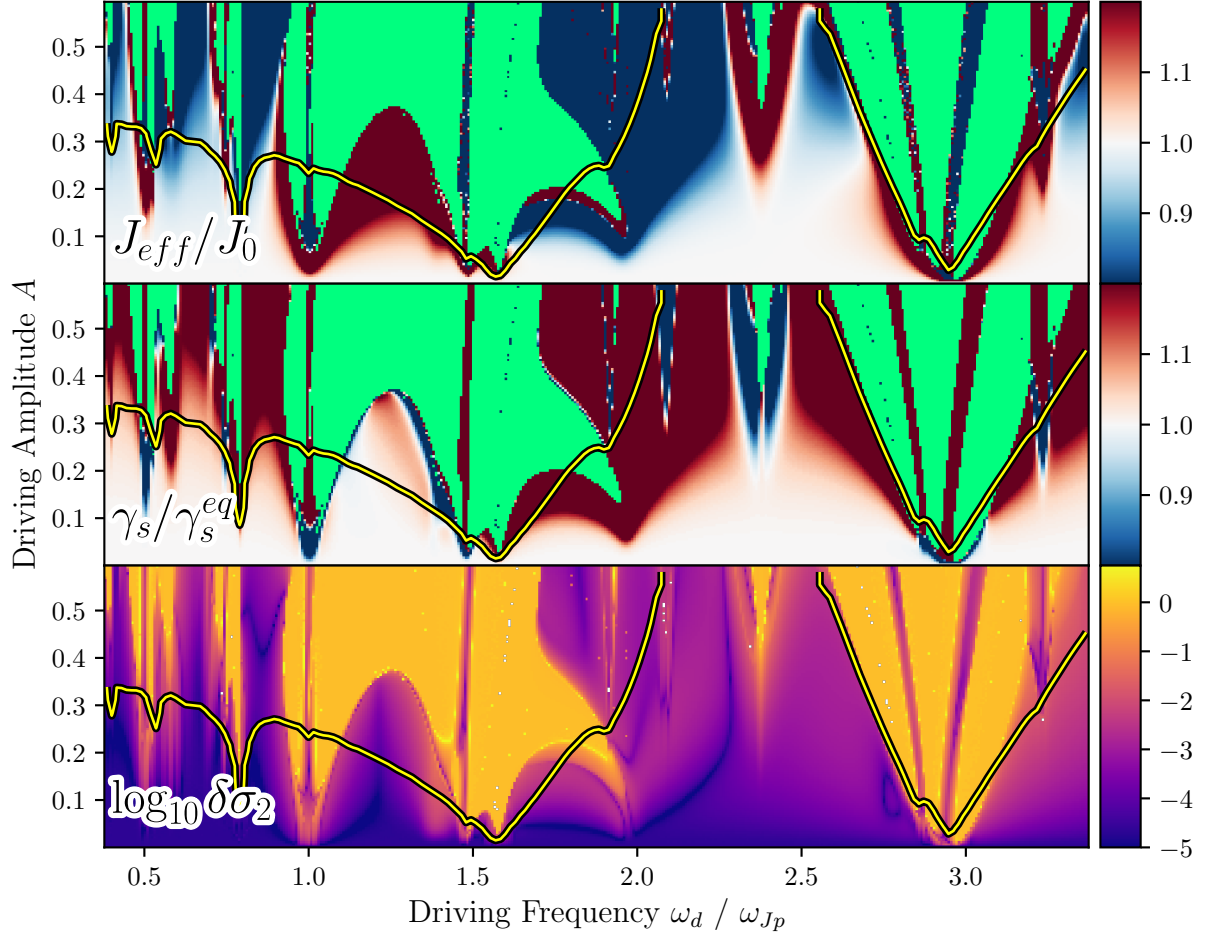
Figure 5.10: **Charge regime parametric driving field**
Parametric driving $f(t) = A\sin(\omega_d t)$ contour plots for $\eta = 1$ at $T = 0$ and $\tilde{\gamma} = 6.9\omega_{\mathrm{Jp}} \times 10^{-2}$. Driving amplitudes above the yellow contour enhance the current fluctuations V_0 by more than 1%. **Top two rows**: Relative change of the effective Josephson energy J_{eff} and the effective relaxation energy $\hbar\gamma_s$ compared to equilibrium. Numerical unstable regions ($\delta\sigma_2 > 5 \times 10^{-2}$) are depicted green. **Bottom row**: relative error on logarithmic scale $\log_{10}\delta\sigma_2$.
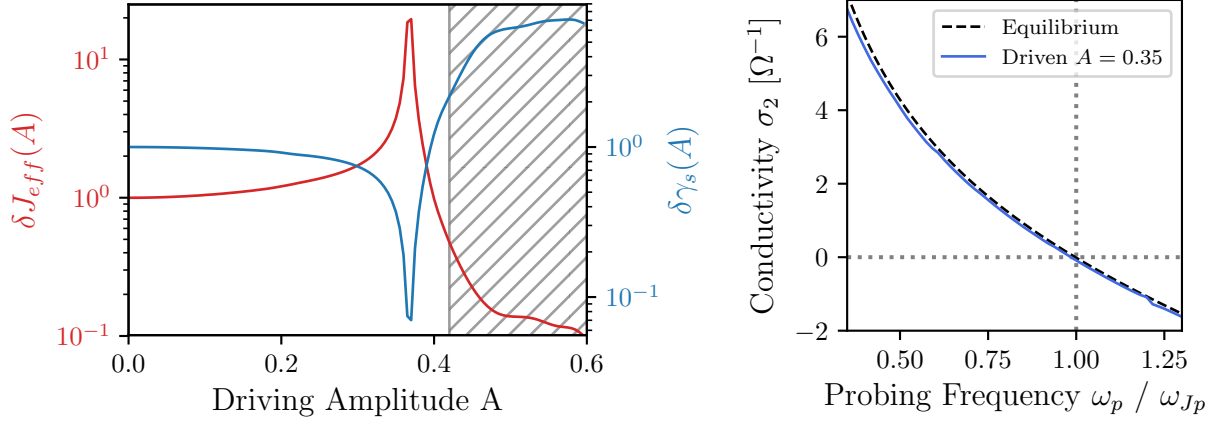
Figure 5.11: **High amplitude driving effective Josephson energy**
left: Relative change of effective Josephson energy δJ_{eff} and relative change of the relaxation energy $\delta\gamma_s$ depicted on logarithmic scale for fixed blue-detuned driving $\omega_d \sim 1.1\omega_{\text{Jp}}$ within the Josephson regime $\eta = 0.11$ at $T = 0$. The damping rate is $\tilde{\gamma} = 8.2\omega_{\text{Jp}} \times 10^{-3}$. At driving amplitudes above $A \gtrsim 0.42$, the relative error exceeds a threshold of $\delta\sigma_2 > 10^{-3}$, which is indicated by the hatched patch. The maximum relative error of $\max \delta\sigma_2 = 3 \times 10^{-2}$ was obtained at $A = 0.6$. **right**: Response of parametrically driven junction at $A = 0.375$ and $\omega_d \sim 1.1\omega_{\text{Jp}}$.

We now consider a fixed driving amplitude near resonance. As already pointed out, blue-detuned pump pulses $\omega_d \sim 1.05\omega_{\text{Jp}}$ lead to an increase of the effective Josephson energy. The enhancement depends on the driving amplitude A as Figure 5.11 shows. By increasing the driving amplitude A, the effective Josephson energy $J_{\text{eff}}(A)$ is enhanced by two orders of magnitude. Even though the junction is underdamped and overdriven, the relaxation regime is stable up to a maximum driving amplitude of $A_{\max} \gtrsim 0.4$. Driving above $A > A_{\max}$ destabilizes the relaxation regime. While the effective Josephson energy increases, the relaxation energy is reduced by $\sim 90\%$. Even though the effective Josephson energy is strongly enhanced, the superconductive response σ_2 near $\omega_p = \omega_{\text{Jp}}$ is reduced. This is due to the fact, that σ_2 is enhanced for probing frequencies below the parametric pole $\omega_p < \omega_* = \omega_d - \omega_{\text{Jp}}$. In the probing spectrum above the pole $\omega_* < \omega_p$, the superconductive response is reduced (see Fig. 5.1).

5.6 Thermal parametric driving field

In the last sections it was pointed out that the energy scales of the relaxation regime are transparent to thermal fluctuations below the plasma energy $2\pi k_b T/\hbar\omega_{\mathrm{Jp}} < 1$. At higher temperatures, excited states become occupied decreasing the Josephson energy J_{eff}. Renormalization of the Josephson energy due to parametric driving at different thermal states is shown in Figure 5.12. At all temperatures, regions of $\delta J_{\mathrm{eff}} > 2$ were observed, even for small driving amplitudes $A \sim 0.1$. The qualitative picture of the $J_{\mathrm{eff}}(A, \omega_d)$ field changes drastically for temperatures $2\pi k_b T/\hbar\omega_{\mathrm{Jp}} > 3$. At $T = 0$, the relaxation energy behaves contrary to the effective Josephson energy, which is only partially the case for high temperatures $2\pi k_b T/\hbar\omega_{\mathrm{Jp}} > 3$. It remains an open question whether a parametrically induced decrease of the relaxation energy $\hbar\gamma_s(T)$ at $2\pi k_b T/\hbar\omega_{\mathrm{Jp}} > 1$ can be associated with an effective cooling or with decreased coupling to the bath.
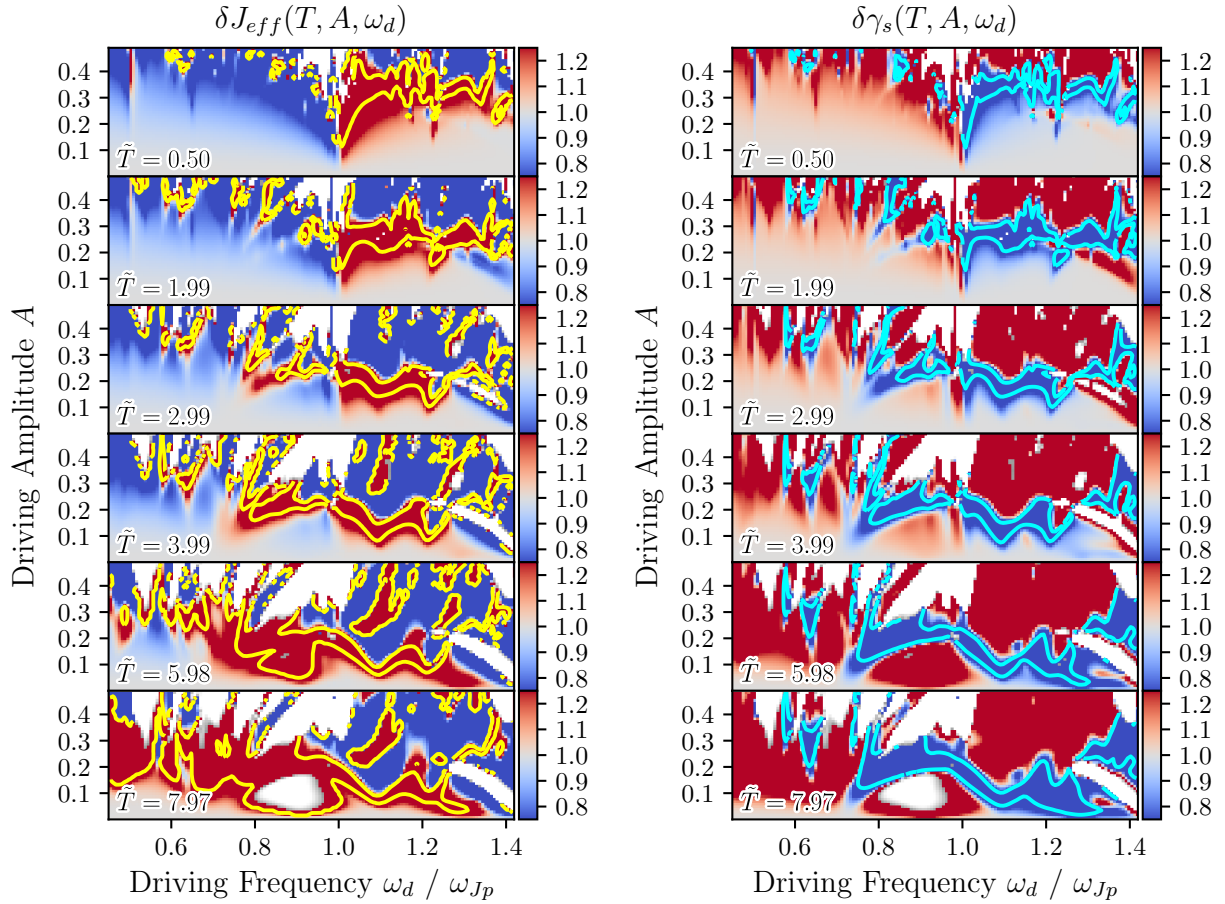
Figure 5.12: **Thermal parametric driving fields**
Parametric driving fields at different thermal states. Unstable regions ($\delta\sigma_2 > 5 \times 10^{-3}$) are depicted white. **left**: Relative change of the effective Josephson energy δJ_{eff}. The yellow contour borders configurations at which the effective Josephson energy doubles $\delta J_{\text{eff}} > 2$ compared to the equilibrium value. **right**: Relative change of the relaxation energy $\delta\gamma_{\text{s}}$. The blue contour borders configurations at which the relaxation energy is halved $\delta\gamma_{\text{s}} < 1/2$ compared to the equilibrium value.

Chapter 6

Conclusion

In this master thesis, a quantum mechanical Josephson junction was analyzed. The model implemented dissipation processes by assuming a weak dipole coupling to an optical heat bath of photons. In the low frequency part of the probing spectrum, the London picture response was obtained. Eventually, as the probing frequency tends towards zero, a relaxation regime emerged. The relaxation regime relates to the uncertainty of modes and connects to decoherence thru interactions with the bath. An effective Josephson energy was defined in terms of the energy scales of the relaxation regime. In the Josephson regime, the effective Josephson energy fulfills the expectations drawn by the London picture. Parametric driving induced a renormalization of both the effective Josephson energy as well as the relaxation energy.

Thermal fluctuations create thermal modes, which are identified by an additional zero-crossing of the imaginary conductivity as well as the appearance of a corresponding relaxation energy scale. Strikingly, thermal modes can be controlled dynamically as they couple to the pump pulse. It was possible to construct a spectrum, where thermal modes couple to the pump pulse such that a strong enhancement of the imaginary conductivity was observed. We want to emphasize that thermal modes are a consequence of the quantized energy spectrum as they belong to transitions between energy states of the system.

For the numerical simulations, two separate software packages were developed. First, the numerical solver of the optical master equation was implemented as a generic library. Modern industry standards, i.e. git and unit testing, ensured a high level of reliability even though optimizations and new features were merged into the library on a regular base. The second part was implemented in a private git repository and contains the concrete implementations of the numerical experiments used in this thesis.

Appendices

Appendix A

Explicit work-item representation

The dissipator $\mathcal{D}A(\omega)$ summands are given by

$$\langle x|A(\omega)\rho A^\dagger(\omega)|y\rangle = \sum_{\omega[ij]}\sum_{\omega[kl]^*} \delta_{ix}\delta_{ky} \sum_{op} \rho_{op}\langle j|o\rangle\langle p|l\rangle = \sum_{\omega[xj]}\sum_{\omega[yl]^*} \rho_{jl}. \qquad (A.1)$$

In the same manner one gets

$$\langle x|A^\dagger(\omega)A(\omega)\rho|y\rangle = \sum_{\omega[ij]}\sum_{\omega[kl]^*}\sum_{mn} \delta_{ix}\delta_{jl}\delta_{km}\delta_{ny}\rho_{mn} = \sum_{\omega[xl]}\sum_{\omega[kl]^*} \rho_{ky} \qquad (A.2)$$

and

$$\langle x|\rho A^\dagger(\omega)A(\omega)|y\rangle = \sum_{mn}\sum_{\omega[ij]}\sum_{\omega[kl]^*} \delta_{xm}\delta_{ni}\delta_{jl}\delta_{ky}\rho_{mn} = \sum_{\omega[ij]}\sum_{\omega[yj]^*} \rho_{xi}. \qquad (A.3)$$

Renaming the indices, the anti-commutator term contributes as

$$\langle x|\{A^\dagger(\omega)A(\omega),\rho\}|y\rangle = \sum_{\omega[xj]}\sum_{\omega[ij]^*} \rho_{iy} + \sum_{\omega[ij]}\sum_{\omega[yj]^*} \rho_{xi}. \qquad (A.4)$$

Appendix B

Minimal qoptical library usage

As an example of the library usage, consider the Harmonic oscillator coupled to an optical bath through the spatial coordinate

$$H = \omega a^\dagger a \otimes \kappa(a^\dagger + a).$$

Due to the spatial coordinate coupling, only the $A(\omega) = a$ dissipator contributes to the dynamics, which leads to a Lindblad master equation of the harmonic oscillator

$$\mathcal{L}\rho = -i\omega[a^\dagger a, \rho] + \gamma_0 w^3(1+n)\mathcal{D}a + \gamma_0 w^3 n\mathcal{D}a^\dagger \qquad \gamma_0 \propto |\kappa|^2. \tag{B.1}$$

The following code evolves the expectation value of the number operator $a^\dagger a$ for two thermal states, thermalizing to the temperature of the heat bath.

```
%matplotlib inline
import numpy as np
import matplotlib.pyplot as plt
from qutip import destroy
import qoptical as qo
qo.QO.DEBUG = True    # let the library print some intersting debug
N, T_bath = 10, 1     # dimH, optical bath thermal state
a = destroy(N)        # annihilation operator
H = a.dag() * a       # HOSCI Hamiltonian (w=1)
# the dipole (a + ad) restricts the jumps to frequency w=1
rs = qo.ReducedSystem(H.full(), dipole=(a + a.dag()).full())
# <n(t)>
nexpect = qo.opmesolve_cl_expect(
    tg=(0, 100, .001),                # time gatter
    reduced_system=rs,
```

```
    t_bath=T_bath,                      # one can also define a list here
    y_0=[.25, .1],                      # one can also define a single value here
    rho0=rs.thermal_state(T=[0, 2]),    # evolve two thermal states
    Oexpect=(a.dag() * a).full(),       # measure <n>
)
plt.axhline(1.0 / (np.exp(1.0 / T_bath) - 1), color="black") # n(T)
plt.plot(nexpect[:, 0].real); plt.plot(nexpect[:, 1].real)
```

Appendix C

Harmonic limit matrix representation

The matrix representation of the operators in the number base are given. The annihilation operator is

$$
a = \begin{pmatrix}
0 & \sqrt{1} & 0 & 0 & 0 \\
0 & 0 & \sqrt{2} & 0 & 0 \\
0 & 0 & 0 & \sqrt{3} & 0 \\
0 & 0 & 0 & 0 & \sqrt{4} \\
0 & 0 & 0 & 0 & 0
\end{pmatrix}.
\tag{C.1}
$$

The number operator is

$$
a = \begin{pmatrix}
0 & 0 & 0 & 0 & 0 \\
0 & 1 & 0 & 0 & 0 \\
0 & 0 & 2 & 0 & 0 \\
0 & 0 & 0 & 3 & 0 \\
0 & 0 & 0 & 0 & 4
\end{pmatrix}.
\tag{C.2}
$$

The squared phase operator is

$$
\left(a + a^\dagger\right)^2 = \begin{pmatrix}
1 & 0 & \sqrt{1*2} & 0 & 0 \\
0 & 3 & 0 & \sqrt{2*3} & 0 \\
\sqrt{1*2} & 0 & 5 & 0 & \sqrt{3*4} \\
0 & \sqrt{2*3} & 0 & 7 & 0 \\
0 & 0 & \sqrt{3*4} & 0 & 9
\end{pmatrix}.
\tag{C.3}
$$

Appendix D

High resolution parametric driving field

We provide a high resolution parametric driving field of the effective Josephson energy and the relaxation energy.
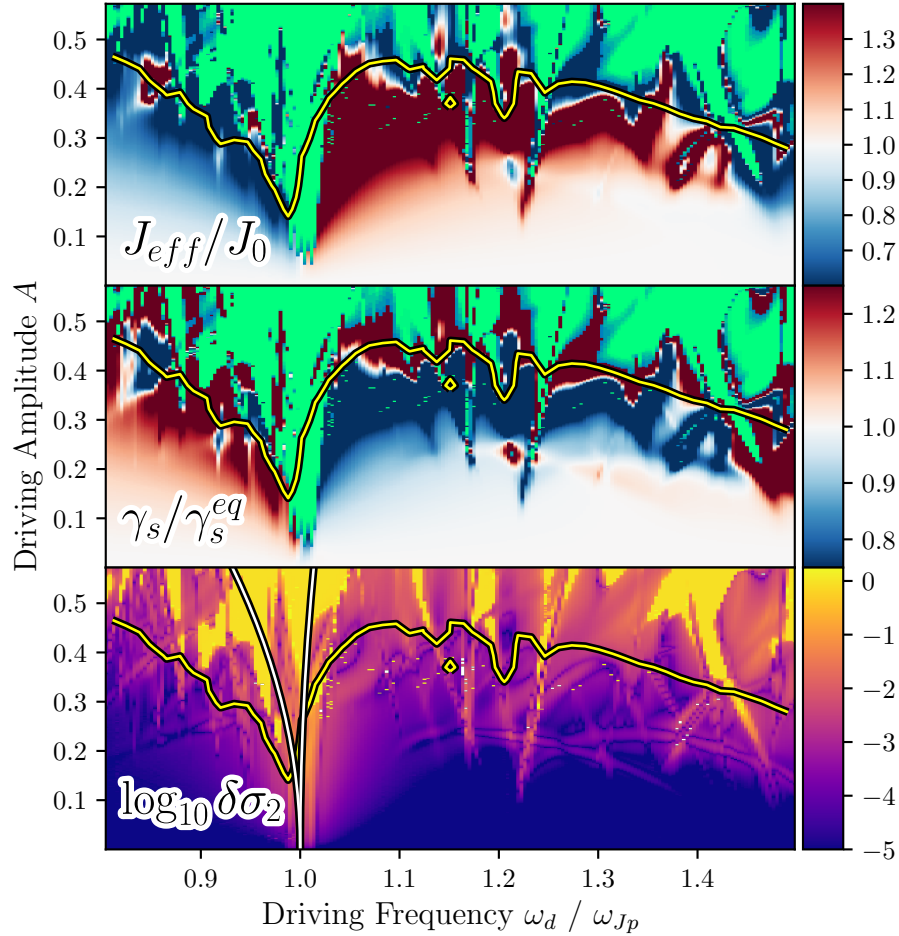
Figure D.1: **Josephson regime parametric driving field**
Parametric driving $f(t) = A \sin(\omega_d t)$ contour plots for $\eta = 0.11$ at $T = 0$ and $\tilde{\gamma} = 8.3 \omega_{\mathrm{Jp}} \times 10^{-3}$. Driving amplitudes above the yellow contour enhance the current fluctuations V_0 by more than 15%. **Top two rows**: Relative change of the effective Josephson energy J_{eff} and the effective relaxation energy $\hbar \gamma_s$ compared to equilibrium. Numerical unstable regions ($\delta \sigma_2 > 5 \times 10^{-3}$) are depicted green. **Bottom row**: relative error on logarithmic scale $\log_{10} \delta \sigma_2$.

Bibliography

[AK07] Robert Alicki and Lendi Karl. *Quantum Dynamical Semigroups and Applications.* Springer-Verlag Berlin Heidelberg, 2007.

[AR63] P. W. Anderson and J. M. Rowell. Probable observation of the josephson superconducting tunneling effect. *Phys. Rev. Lett.*, 10:230–232, Mar 1963.

[Arm09] N. P. Armitage. Electrodynamics of correlated electron systems. *arXiv e-prints*, page arXiv:0908.1126, Aug 2009.

[Bar55] J. Bardeen. Theory of the meissner effect in superconductors. *Phys. Rev.*, 97:1724–1725, Mar 1955.

[BB05] Gregory Baker and James Blackburn. *The Pendulum - A Case Study in Physics.* Oxford University Press Inc., New York, 2005.

[BCS57a] J. Bardeen, L. N. Cooper, and J. R. Schrieffer. Microscopic theory of superconductivity. *Phys. Rev.*, 106:162–164, Apr 1957.

[BCS57b] J. Bardeen, L. N. Cooper, and J. R. Schrieffer. Theory of superconductivity. *Phys. Rev.*, 108:1175–1204, Dec 1957.

[BM86] J. G. Bednorz and K. A. Müller. Possible hightc superconductivity in the balacuo system. *Zeitschrift für Physik B Condensed Matter*, 64(2):189–193, Jun 1986.

[BP02] Heinz-Peter Breuer and Francesco Petruccione. *The theory of open quantum systems.* Oxford University Press Inc., New York, 2002.

[Car02] Howard Carmichael. *Statistical Methods in Quantum Optics 1*, volume 1. Springer-Verlag Berlin Heidelberg GmbH, 2 edition, 2002.

[CB12] M. D. Croitoru and A. I. Buzdin. Extended Lawrence-Doniach model: The temperature evolution of the in-plane magnetic field anisotropy. *Physical Review B*, 86(22):224508, Dec 2012.

[Coo56]   Leon N. Cooper. Bound electron pairs in a degenerate fermi gas. *Phys. Rev.*, 104:1189–1190, Nov 1956.

[DDK11]   van Delft Dirk and Peter Kes. The discovery of superconductivity. *Europhysics News*, 63, 01 2011.

[DF61]   Bascom S. Deaver and William M. Fairbank. Experimental evidence for quantized flux in superconducting cylinders. *Phys. Rev. Lett.*, 7:43–46, Jul 1961.

[Dru00a] P. Drude. Zur elektronentheorie der metalle. *Annalen der Physik*, 306(3):566–613, 1900.

[Dru00b] P. Drude. Zur elektronentheorie der metalle; ii. teil. galvanomagnetische und thermomagnetische effecte. *Annalen der Physik*, 308(11):369–402, 1900.

[FTD+11] D. Fausti, R. I. Tobey, N. Dean, S. Kaiser, A. Dienst, M. C. Hoffmann, S. Pyon, T. Takayama, H. Takagi, and A. Cavalleri. Light-induced superconductivity in a stripe-ordered cuprate. *Science*, 331(6014):189–191, 2011.

[Gab89]   Lippmann Gabriel. Sur une loi générale de l'induction, dans les circuits dénués de résistance. *Comptes rendus hebdomadaires des séances de l'Académie des Sciences 109*, page 251255, 1889.

[Gin55]   V. L. Ginzburg. On the theory of superconductivity. *Il Nuovo Cimento (1955-1965)*, 2(6):1234–1250, Dec 1955.

[GMB64]   L. P. GOR'KOV and T. K. MELIK-BARKHUDAROV. Microscopic derivation of the ginzburg-landau equations for an anisotropic superconductor. *SOVIET PHYSICS JETP*, 18, 1964.

[HKN+14] Wenli Hu, Stefan Kaiser, Daniele Nicoletti, Cassandra Hunt, I Gierz, M C Hoffmann, Matthieu Le Tacon, T Loew, B Keimer, and Andrea Cavalleri. Optically enhanced coherent transport in yba2cu3o6.5 by ultrafast redistribution of interlayer coupling. *Nature materials*, 13, 05 2014.

[Hom18]   Guido F. Homann. Optically Enhanced Interlayer Tunneling in High-Temperature Superconductors. Master's thesis, University of Hamburg, Nov 2018.

[HQ01]   Karl-Heinz Hoffmann and Tang Qi. *Ginzburg-Landau Phase Transition Theory and Superconductivity*. Springer Basel AG, 2001.

[HZR+15] R. Höppner, B. Zhu, T. Rexin, A. Cavalleri, and L. Mathey. Redistribution of phase fluctuations in a periodically driven cuprate superconductor. *Physical Review B*, 91(10):104507, Mar 2015.

[JNN12] J. R. Johansson, P. D. Nation, and Franco Nori. QuTiP: An open-source Python framework for the dynamics of open quantum systems. *Computer Physics Communications*, 183(8):1760–1772, Aug 2012.

[JNN13] J. R. Johansson, P. D. Nation, and Franco Nori. QuTiP 2: A Python framework for the dynamics of open quantum systems. *Computer Physics Communications*, 184(4):1234–1240, Apr 2013.

[Jos62] B.D. Josephson. Possible new effects in superconductive tunnelling. *Physics Letters*, 1(7):251 – 253, 1962.

[Jos74] B. D. Josephson. The discovery of tunnelling supercurrents. *Rev. Mod. Phys.*, 46:251–254, Apr 1974.

[Kle74] M.J. Klein. The historical origins of the van der waals equation. *Physica*, 73(1):28 – 47, 1974.

[LEE] C. H. LEES. The liquefaction of gases. 104:247–248.

[Leg06] Anthony J. Leggett. What DO we know about high tc? 2(3):134–136, 2006.

[Lin76] G. Lindblad. On the generators of quantum dynamical semigroups. *Comm. Math. Phys.*, 48(2):119–130, 1976.

[LL97] Lew D. Landau and Jewgeni M. Lifschitz. *Lehrbuch der theoretischen Physik - Mechanik*. Harri Deutsch, 14 edition, 1997.

[LLL35] F. London, H. London, and Frederick Alexander Lindemann. The electromagnetic equations of the supraconductor. *Proceedings of the Royal Society of London. Series A - Mathematical and Physical Sciences*, 149(866):71–88, 1935.

[Lon48] F. London. On the problem of the molecular theory of superconductivity. *Phys. Rev.*, 74:562–573, Sep 1948.

[McC68] D. E. McCumber. Effect of ac impedance on dc voltagecurrent characteristics of superconductor weaklink junctions. *Journal of Applied Physics*, 39(7):3113–3118, 1968.

[MO33] W. Meissner and R. Ochsenfeld. Ein neuer effekt bei eintritt der supraleitfähigkeit. *Naturwissenschaften*, 21(44):787–788, Nov 1933.

[NT08] Mikio Nakahara and Ohmi Tetsuo. *QUANTUM COMPUTING - From Linear Algebra to Physical Realizations*. CRC-Press, 2008.

[OCM16a] Jun-ichi Okamoto, Andrea Cavalleri, and Ludwig Mathey. Theory of Enhanced Interlayer Tunneling in Optically Driven High-T_c Superconductors. *Physical Review Letters*, 117:227001, Nov 2016.

[OCM16b] Jun-ichi Okamoto, Andrea Cavalleri, and Ludwig Mathey. Theory of Enhanced Interlayer Tunneling in Optically Driven High-T_c Superconductors. *Physical Review Letters*, 117:227001, Nov 2016.

[OHCM17] Jun-ichi Okamoto, Wanzheng Hu, Andrea Cavalleri, and Ludwig Mathey. Transiently enhanced interlayer tunneling in optically driven high-T_c superconductors. *Physical Review B*, 96:144505, Oct 2017.

[Onn13] H. Kamerlingh Onnes. Investigations into the properties of substances at low temperatures, which have led, amongst other things, to the preparation of liquid helium. *Nobel Lecture*, 12 1913.

[Onn91] H. Kamerlingh Onnes. *Further Experiments with Liquid Helium. D. On the Change of the Electrical Resistance of Pure Metals at very low Temperatures, etc. V. The Disappearance of the resistance of mercury*, pages 264–266. Springer Netherlands, Dordrecht, 1991.

[PB53] Alfred Brian Pippard and William Lawrence Bragg. An experimental and theoretical study of the relation between magnetic field and current in a superconductor. *Proceedings of the Royal Society of London. Series A. Mathematical and Physical Sciences*, 216(1127):547–568, 1953.

[PTVF07] William H. Press, Saul A. Teukolsky, William T. Vetterling, and Brian P. Flannery. *Numerical Recipes 3rd Edition: The Art of Scientific Computing*. Cambridge University Press, New York, NY, USA, 3 edition, 2007.

[RH12] ngel Rivas and Susana Huelga. *Open Quantum Systems - An Introduction*. Springer Heidelberg Dordrecht London New York, 2012.

[Sch07] Franz Schwabl. *Quantenmechanik (QMI)*. Springer-Verlag Berlin Heidelberg New York, 7 edition, 2007.

[Sch08] Franz Schwabl. *Quantenmechanik fur Fortgeschrittene (QMII)*. Springer-Verlag Berlin Heidelberg, 5 edition, 2008.

[Tan14]   Yoshitaka Tanimura. Reduced hierarchical equations of motion in real and imaginary time: Correlated initial states and thermodynamic quantities. *Journal of Chemical Physics*, 141(4):044114, Jul 2014.

[Tin96]   Michael Tinkham. *Introduction to Superconductivity*. McGraw-Hill Inc.,US, 2 edition, 1996.

[WAT⁺87]   M. K. Wu, J. R. Ashburn, C. J. Torng, P. H. Hor, R. L. Meng, L. Gao, Z. J. Huang, Y. Q. Wang, and C. W. Chu. Superconductivity at 93 k in a new mixed-phase y-ba-cu-o compound system at ambient pressure. *Phys. Rev. Lett.*, 58:908–910, Mar 1987.

[Wei99]   Ulrich Weiss. *The theory of open quantum systems (2nd edition)*, volume 10. World Scientific Publishing Co. Pte. Ltd., 2 edition, 1999.

[Wis03]   Jaime Wisniak. James dewar more than a flask. *Indian Journal of Chemical Technology*, 10:424–434, 07 2003.

Acknowledgements

Eidesstattliche Erklärung

Ich versichere, dass ich die beigefügte schriftliche Masterarbeit selbstständig angefertigt und keine anderen als die angegebenen Hilfsmittel benutzt habe. Alle Stellen, die dem Wortlaut oder dem Sinn nach anderen Werken entnommen sind, habe ich in jedem einzelnen Fall unter genauer Angabe der Quelle deutlich als Entlehnung kenntlich gemacht. Dies gilt auch für alle Informationen, die dem Internet oder anderer elektronischer Datensammlungen entnommen wurden. Ich erkläre ferner, dass die von mir angefertigte Masterarbeit in gleicher oder ähnlicher Fassung noch nicht Bestandteil einer Studien- oder Prüfungsleistung im Rahmen meines Studiums war. Die von mir eingereichte schriftliche Fassung entspricht jener auf dem elektronischen Speichermedium.

Ich bin damit einverstanden, dass die Masterarbeit veröffentlicht wird.

Hamburg, den 03.06.2019